Search for Invisible Decays of Dark Photon at Belle II

by

Miho Wakai

MSci, King's College London, 2019

A THESIS SUBMITTED IN PARTIAL FULFILLMENT OF
THE REQUIREMENTS FOR THE DEGREE OF

MASTER OF SCIENCE

in

The Faculty of Graduate and Postdoctoral Studies

(Physics)

THE UNIVERSITY OF BRITISH COLUMBIA

(Vancouver)

October 2021

The following individuals certify that they have read, and recommend to the Faculty of Graduate and Postdoctoral Studies for acceptance, the thesis entitled:

Search for Invisible Decays of Dark Photon at Belle II

submitted by **Miho Wakai** in partial fulfillment of the requirements for the degree of **Master of Science** in **Physics**.

Examining Committee:

Christopher Hearty, Physics and Astronomy, UBC
Supervisor

Janis McKenna, Physics and Astronomy, UBC
Additional Examiner

Abstract

The Standard Model of particle physics displays a good description of the nature of fundamental particles. However, there are some inconsistencies between theory and experimental evidence. One of the observations made through astronomy and cosmology but is not explained by the Standard Model is dark matter. Many theories have been made to explain dark matter, which includes the dark photon particle. The dark photon is a hypothetical particle thought to exist as a mediator between the Standard Model photon and dark matter particles. The dark photons can be produced at an electron-positron collider like the Belle II experiment, located at the KEK particle physics facility. The work presented shows the first attempts of the search for dark photons with invisible decays, where studies on background were conducted for low dark photon masses. This involved understanding the different backgrounds for dark photon events, the geometry and efficiency of the main sub-detectors, and making the final background estimates. In addition, discrepancies between data and Monte Carlo events for the background control sample were found due to detector imperfections, which are also summarised here.

Lay Summary

The Standard Model of particles physics is a model describing the nature of fundamental particles. However, there are some mysterious effects observed in nature that the Standard Model does not perfectly encapsulate. One of these observations is matter which is non-luminous, and a new type of particle, the dark photon, is theorised to exist to provide understanding. The work presented here describes the early stages of the search for this particle at the Belle II detector.

Preface

This dissertation is based on data of Belle II experiment, which is a large international collaboration. The result is original and unpublished.

The idea of searching for a dark photon using the Belle II detector was suggested by my supervisor Prof. Christopher Hearty. The design of the analysis was done by the dark photon group at Belle II, which consists of Prof. Hearty, Prof. Torben Ferber, Dr. Sam Cunliffe, and myself. The production of signal Monte Carlo events was done by Dr. Cunliffe, while the data and background Monte Carlo events were produced by the Belle II collaboration. The beams are provided by the SuperKEKB accelerator. The data used here was produced between 2019 to 2020 by the Belle II collaboration, and I have not been part of the data taking during my project. Figure 3.3 was produced by Prof. Hearty, figure 3.4 was produced by Dr. Cunliffe, while the rest of the figures in the analysis were produced by myself.

Table of Contents

Abstract iii

Lay Summary iv

Preface v

Table of Contents vi

List of Tables viii

List of Figures ix

List of Symbols xi

Glossary xii

Acknowledgements xiv

1 Theoretical overview 1
- 1.1 The Standard Model of particle physics 1
- 1.2 Dark matter 2
- 1.3 Dark photon 6

2 The Belle II experiment 8
- 2.1 SuperKEKB 8
- 2.2 The Belle II detector 10
  - 2.2.1 Vertex detector 12
  - 2.2.2 Central drift chamber (CDC) 13
  - 2.2.3 Particle identification system (PID) 14
  - 2.2.4 Electromagnetic calorimeter (ECL) 15
  - 2.2.5 Superconducting magnets 21
  - 2.2.6 K_L muon detector (KLM) 21
- 2.3 Trigger 24

3 Search for dark photons 25
3.1 Analysis overview 25
3.2 Efficiency studies 31
3.3 Comparison between MC and data 36
3.4 Bhabha events 40
3.5 Changing ECL geometry 42
3.6 Signal analysis 48
3.7 Cosmics and pin diode studies 56

4 Conclusions 67
4.1 Dark photon search at Belle II 67

Bibliography 69

Appendix

A Analysis on cosmic events 74
A.1 ZernikeMVA and KLM cuts for data 74
A.2 ZernikeMVA and KLM cuts for cosmic events 76

List of Tables

3.1 Summary of type of MC files used. 30
3.2 Summary of type of data files used. 30
3.3 KLM efficiency for Proc11 Exp10 data and MC. 38
3.4 Results of Kolmogorov–Smirnov test for Exp16 and Ep18 cosmic events and Buckets 9-15 Exp12 data. 61
3.5 Results and validation ratio of prediction for all methods and cuts in Buckets 9-15 Exp12 data. 65

A.1 Table for the number of events which pass and fail the ZernikeMVA and KLM cut for Buckets 9-15 Exp 12 data. 75
A.2 Table for the number of events which pass and fail the ZernikeMVA and KLM cut for cosmics events in Exp16 and Exp18. 77

List of Figures

1.1 The Standard Model of particle physics. 2
1.2 The rotation curves for galaxies M31, M101, and M81. 3
1.3 Kinetic mixing of the SM photon and the dark photon A' at the one-loop level. 7

2.1 The Super KEKB accelerator. 9
2.2 The Belle II detector 10
2.3 Cross sectional view of the Belle II detector 11
2.4 Geometry overview of the ECL at Belle II. 17
2.5 Cross sectional view of the ECL with theta IDs. 18
2.6 Schematic drawing of a cascade of photon showers within one crystal of the ECL. 18
2.7 Schematic drawing of the electronics wrapping the crystal of the ECL. 19
2.8 Geometry overview of the KLM at Belle II. 23

3.1 Feynman diagram of the invisibly decaying dark photon event. 25
3.2 Sensitivity and constraints of the dark photon at Belle II in the coupling strength and mass parameter space. 26
3.3 Trigger efficiency for 0.5 GeV single photon events as a function of CoM energy of the photon using a radiative muon control sample. 27
3.4 CoM energy against lab frame theta of a photon from MC background events. 28
3.5 Number of photons per crystal in ECL in MC13b Proc11 Exp10 for different leakage energies. 33
3.6 Percentage of photons per crystal in ECL which were matched with KLM clusters in MC13b Proc11 Exp10 for different leakage energies. 35
3.7 Ratios of KLM efficiencies for Proc11 Exp10 data and MC. . 38
3.8 Number of probe photons in ECL matched with a KLM cluster for Proc10 Exp8 and Bucket8 Exp10 data. 39

3.9 CoM energy of probe photons in Proc10 Exp8 and Proc11 Exp10 data and MC. 40
3.10 Number of probe particles in ECL as a function of CoM energy for MC13b Proc11 Exp10. 41
3.11 High leakage probe particles as a function of theta ID for MC13b Proc11 Exp10. 42
3.12 Local theta of high leakage probe photons for Proc11 Exp10 data and MC. 44
3.13 Local phi of high leakage probe photons for Proc11 Exp10 data and MC. 44
3.14 CoM energy of probe photon for MC13a, data Bucket8 Exp10, and shifted crystal geometry. 45
3.15 UncorrectedE21/E of probe photons for MC13a, data Bucket8 Exp10, and shifted crystal geometry. 47
3.16 Ratio of high leakage probe photons to all probe photons as a function of tag theta ID for Proc11 Exp10 data and MC. . 49
3.17 Ratio of KLM probes to ECL probes as a function of tag theta ID for Proc11 Exp10 data and MC. 50
3.18 Theta ID of candidate photon against most back-to-back photon for MC13b Proc11 Exp10. 52
3.19 Punzi figure of merit for energy of second most energetic photon. 53
3.20 MC13b Proc11 Exp10 and MC13b Buckets 9-15 Exp12 comparison with relevant variables using the control sample of $e^+e^- \to \gamma\gamma$ events. 55
3.21 Energy of candidate photon for Bucket 9-15 Exp12 data and MC. 56
3.22 ZernikeMVA distribution of candidate photon for signal, cosmic, data, and MC $e^+e^- \to \gamma\gamma$ events. 59
3.23 Time distribution of candidate photon for signal, cosmic, data, and MC $e^+e^- \to \gamma\gamma$ events. 59
3.24 Number of KLM layers against opening angle of best KLM cluster with candidate photon for signal, cosmic, data, and MC $e^+e^- \to \gamma\gamma$ events. 60
3.25 CoM energy of candidate photon for cosmic and data events with different cuts. 63
3.26 CoM energy of candidate photon for Buckets 9-15 Exp12 data with different cuts. 65

List of Symbols

A'	Dark photon
θ	Polar angle
$e^{\pm}$	Electron or positron
ϵ	Kinetic mixing of dark photon and SM photon
γ	Photon
q	Quark
Z	Z boson
π	Pion
K	Kaon
μ	Muon
η	Eta meson
ϕ	Azimuthal angle
Υ	Upsilon meson

Glossary

ARICH aerogel ring-imaging Cherenkov

BDT boosted decision tree

CDC central drift chamber

CMB cosmic microwave background

CoM center of mass

CP charge parity

CsI(Tl) thallium-doped cesium iodide

DAQ data acquisition

DEPFET depleted field effect transistor

DM dark matter

ECL electromagnetic calorimeter

EM electromagnetic

GDL general decision logic

GRL general reconstruction logic

HER high energy ring

HLT high level trigger

IP interaction point

KLM K_L muon detector

L1 level 1

LER low energy ring

LINAC linear accelerator

MC Monte Carlo

MCP-PMT micro-channel-plate-photomultiplier tube

PID particle identification

PXD pixel detector

QCD	quantum chromodynamics
RPC	resistive plate chambers
SiPM	silicon photomultipliers
SM	standard model
SVD	silicon vertex detector
TOP	time of propagation
WIMP	weakly interacting massive particles

Acknowledgements

I would like to thank my supervisor Chris Hearty, for always being supportive and present during my project. I look forward to working more and learning more from you. I would also like to thank Alon Hershenhorn and Ewan Hill for their kindness in helping me. Torben Ferber and Sam Cunliffe are also people that I've had a great privilege of working with and gained a lot of knowledge from them. This project came into place with the help of brilliant people whom I am greatly appreciative of their presence in my life.

Chapter 1

Theoretical overview

1.1 The Standard Model of particle physics

The standard model (SM) of elementary particles physics represents our current understanding of fundamental particles and their interactions. This theoretical framework is a unified gauge theory of electroweak and strong interactions, representing three of the four fundamental forces in our universe. The SM shows how matter can be split into two different types; twelve spin $\frac{1}{2}$ fermions which are the building blocks of matter, and four spin 1 gauge bosons which are force carrying particles. In addition, there is the spin 0 Higgs boson which gives mass to the massive particles. A summary of these particles can be seen in figure 1.1.

The SM, which is a relativistic quantum field theory, has proven over time its consistency to describe the nature of particle physics. Although the SM was developed in the early 1970s, it was only afterwards that some of the particles were discovered experimentally, with Higgs boson being the most recent discovery in 2012.

However, the SM is not perfect. There are empirical phenomena that cannot be understood nor explained with the SM. An example of this is the baryon asymmetry, which comes from the in-balance between the amount of baryonic matter and anti-matter observed in our current universe. Another example is dark matter (DM) which consists of 26% of the universe yet its constitutes are unknown. This is described in detail in section 1.2. In addition, there is the Strong QCD problem. In quantum chromodynamics (QCD), the SM theoretically shows that the strong force may violate charge parity (CP) conservation. However this has never been experimentally observed. As a solution to this problem, a hypothetical particle called the axion has been theorised [1], although has never been detected.

There has been an ongoing pursuit of solving the inconsistencies found between theory and empirical evidence within the SM. The dark photon search at the Belle II experiment is also contributing to this effort, which the analysis is described in chapter 3.

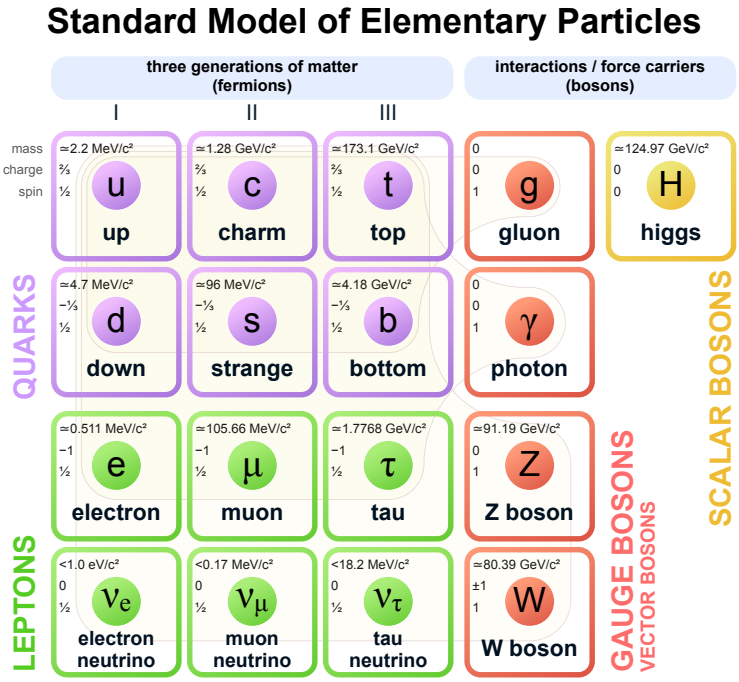

Figure 1.1: The summary of the particles in the Standard Model. There are 6 quarks and leptons, grouped together as fermions which are the building blocks of matter. There are 4 gauge bosons which carry the 3 forces, and the Higgs Boson which gives off mass to the massive gauge bosons [2].

1.2 Dark matter

One of the largest motivations for new physics searches is to understand dark matter. There is a substantial amount of evidence in astrophysical and cosmological data for dark matter, yet very little of its properties are known. DM is considered to interact through only the gravitational force, and does not interact through the strong and electroweak forces. DM accounts for 26% of the total matter in the universe, while SM matter accounts for 5%. There are three main experimental observations which shows evidence for dark matter; discrepancy of rotational speed and observed mass, cosmic microwave background, and gravitational lensing.

DM was first theorised in 1933 when Fritz Zwicky observed a discrepancy between the estimated mass from the motion of galaxies and stars in the Coma cluster, and the mass from the observed luminosity [3]. The discrepancy demonstrated how there was matter in the universe that could not be observed through normal light, hence the term dark matter. Vera Rubin and Kent Ford became the first to observe direct evidence of dark matter in the 1970s, when studying the spectral lights from stars [4]. By studying the Doppler shifts of stars, Rubin and Ford calculated the orbital speeds of stars among different parts of the galaxy. From Newtonian law, the rotational velocity of a star should fall when increasing the distance from the Sun. However, the results indicated that the stars further from the Sun were rotating just as fast as those nearby, showing a flat distribution between the distance and rotational speed. This flat distribution can be observed in figure 1.2, where the different curves represent different galaxies. The visible mass was not enough to account the rapid rotational speeds, hence the calculations signified that there must be missing mass for the observations to make sense. This became the start of the search for dark matter, with many different observations following to confirm its existence.

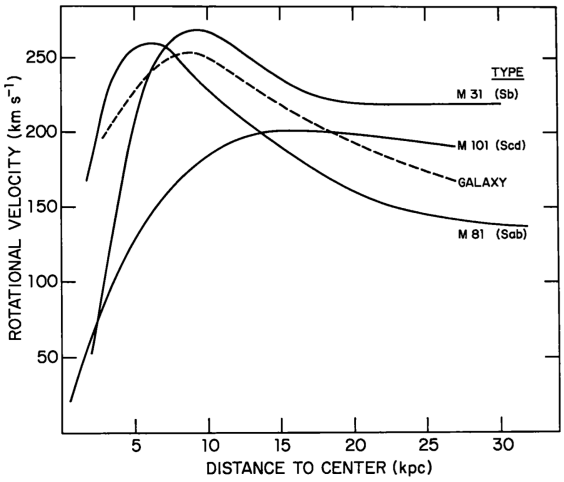

Figure 1.2: The rotation curves for galaxies M31, M101, and M81. Research was conducted in 1973 by A. H. Rots and M. Roberts [5].

Another evidence used to argue for DM is the cosmic microwave background (CMB). The CMB is the remnants of the heat from the Big Bang that exist today in the form of electromagnetic waves. The CMB has anisotropic characteristics, which depicts how there were deviations in the microwaves 380,000 years after the Big Bang. The anisotropy can show the densities of non-baryonic matter in the universe. In order to look at dark matter, the spatial anisotropies were turned into an angular power spectrum. There were three acoustic peaks in the spectrum, showing the main composites of the universe; dark energy, dark matter, and ordinary matter. The amplitudes of these peaks also depend on the amount of density, leading to estimates on density distributions. Currently, the most accurate measurements of the cosmological density parameters derived from the CMB come from the Planck satellite results, with dark matter content being 26.8%, dark energy being 68.3%, and normal matter being 4.9% of the total energy matter density of the universe [6].

Gravitational lensing has also been a strong indicator for dark matter. Gravitational lensing is a deflection of photons as they pass through a gravitational field with massive objects, due to general relativity. The first observation was made in 1919 when stars in the Hyades star cluster appeared to have altered their position behind the Sun during the solar eclipse. This is due to the light being bent by the mass of the Sun. The dark matter detection comes into play when light from distant galaxies is distorted when they pass by a clump of dark matter. One of the most famous gravitational lensing observations was made by NASA's Chandra X-Ray Observatory of the Bullet Cluster. The Bullet Cluster was formed after two large clusters of galaxies collided. When the concentration of mass was studied using gravitational lensing, there was other invisible matter which was different from the hot gas initially observed. In addition, when the hot gas of each of the galaxies passed through one another, it was slowed down by drag force. The invisible matter however was at a location further away from the center than the hot gas. This matter was concluded to be dark matter, as it did not interact with anything other than gravity, and hence was not affected by the drag force.

Dark matter particles can be understood indirectly from the astrophysical and cosmological observations listed above. However, in order to measure the properties of dark matter such as its mass, coupling, and cross section with ordinary matter, different detection methods for dark matter in particle physics have been pursued. There are currently three main methods; direct detection, indirect detection, and direct production.

Direct detection is a popular method for detection weakly interacting massive particles (WIMP). WIMPs are slow moving dark matter candidates and are thought to have a mass below the $\mathrm{TeV/c^2}$ range. Direct detection looks at WIMPs elastically scattering off an atomic nucleus, which the rise in nuclear recoil from the momentum transfer becomes the signature. The nuclear recoil can be detected in mainly two ways; from ionization through scintillation light in iodide crystals and noble gas detectors, or by phonons and ionization produced in solid state detectors.

Indirect detection relies on detecting anomalous flux of neutrinos, cosmics rays, and photons. Ground based telescopes, balloon borne detectors, and space based experiments are the main methods of pursuing indirect detection [7]. The three types of dark matter produced in indirect detection are dark matter self annihilations, decays, and conversions.

Dark matter annihilation events are thought to occur in the center of the Sun or Earth, and neutrinos are the only particles that are able to leave their dense interiors [8]. Experiments such as IceCube, Super-Kamiokande, and ANTARES are looking for these signals. Dark matter may also be observed through gamma rays from annihilation or decay events. Due to their electrically neutral feature, gamma rays will not be deflected by magnetic fields and can be traced back to their origin, unlike charged particles. There is an excess amount of gamma rays observed by the Fermi Large Aread Telescope, which may have come from dark matter sources [9]. Positron excess from PAMELA [10] and AMS [11] may also be explained through dark matter annihilations, however conventional explanations such as pulsars or supernova remnants are also possible.

Dark matter decays could also be detected. A small fraction of dark matter particles are considered to decay which involves an emission of a photon. Various dark matter models may be identified through different characteristics of the photon emission. Light dark matter, gravitinos, neutralinos, and sterile neutrinos which are all candidates of dark matter have been studied for the possibility of decay.

Dark matter conversions have also been studied where hypothetical particles called axions are thought to convert into photons. Experiments such as the ADMX attempts this search by using a strong magnetic field to convert dark matter axions into microwave photons [12].

Finally, dark matter is also believed to be created through SM interactions, where the particles colliding annihilate into dark matter particles. Theories suggest that dark matter may not just be one type of particle, but a bundle of different particles, where all of these particles belong to the dark sector. The dark sector particles are considered to be neutral un-

der SM forces but is charged under DM forces. Particles that belong to the dark sector may be dark matter candidates themselves, or act as mediators. Different dark matter models have been considered within the dark sector, where there could be different portals between DM and SM particles. Such models include a vector, scalar, axial vector, or a pseudo scalar particle. Examples of these are the Z' boson, dark Higgs boson, and the Axion-like particle which collider experiments have been searching for. These particles are thought to interact feebly with the SM particles, due to their small couplings strengths. Most searches involve missing energy, where the final state becomes invisible. There currently has been no success at finding dark sector particles at collider experiments.

1.3 Dark photon

Throughout the quest to understand dark matter, a new possibility of its nature has arisen. The possibility suggests that dark matter particles may interact with other dark matter particles through a "dark force" which is analogous to the electromagnetic force in the SM. This unknown dark force allows interactions through a hidden charge within the dark sector. If this were true, there would need to be a massive gauge boson acting as a mediator for this new hidden symmetry. This is analogous to what the SM photon does by carrying the electromagnetic force. This gauge boson is called the dark photon.

The dark photon A' was first introduced by Holdom [13], who theorised the existence of a spin-one gauge boson becoming a mediator for a hidden $U(1)$ symmetry. The crucial point of the A' is that it kinetically mixes with the SM hypercharge $U(1)$, meaning that the interaction between the dark and SM photon could provide "portal" through which this hidden sector could be accessed. The coupling of the dark photon to the electric charge is considered to be suppressed, roughly in the 10^{-12} to 10^{-2} range [14]. Figure 1.3 demonstrates the kinetic mixing mechanism between the SM photon and A' through a Feynman diagram. This can happen if a doublet of the hidden $\Psi(\Psi')$ dark matter particles were to exist, which are charged under both the SM hypercharge gauge group and the dark symmetry [14].

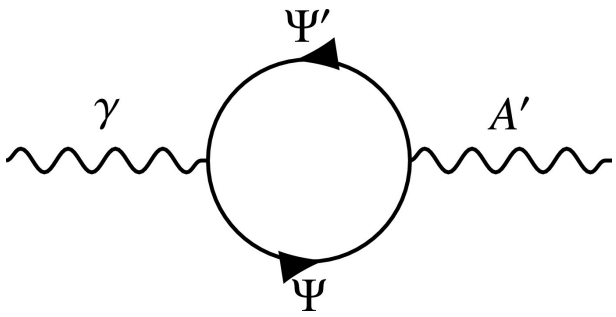

Figure 1.3: Feynman diagram of the kinetic mixing of the SM photon and the dark photon A' at the one-loop level [14]. The diagram indicates the possibility of an interaction between the SM photon γ and the dark photon A'. The $\Psi(\Psi')$ indicates a doublet of dark matter particles, charged under both the SM hypercharge gauge group and the dark symmetry.

For minimal dark photon model, where the particle is cold and slow moving, it currently has three unknown parameters; the strength of the kinetic mixing ϵ, the dark photon mass $m_{A'}$, and the decay branching fraction of the dark photon into invisible dark sector final states $A' \to \chi\bar{\chi}$ [15].

Dark photon events can be largely split into two types; dark photons decaying visibly to SM particles, and dark photons decaying invisibly to dark sector particles. The former will only happen if the latter is kinematically forbidden. For visibly decaying events, depending on the mixing strength, it can either decay immediately at the production point of the dark photon, or have a displaced decay point.

Different signatures for producing the dark photon have been pursued in various particle accelerator facilities which are listed below [15].

- $eZ' \to eZA'$ and $pZ \to pZA'$ (Bremsstrahlung event)
- $e^+e^- \to A'\gamma$
- $q\bar{q} \to A'$ (Drell-Yan event)
- $\pi^0 \to A'\gamma$ or $\eta \to A'\gamma$
- V(QCD vector meson of ω, ρ, ϕ) $\to A'$ (mixing of A')

Chapter 2

The Belle II experiment

2.1 SuperKEKB

The SuperKEKB collider is located in Tsukuba, Japan, where e^+e^- collisions happen underground through a 3 km circumference ring. The SuperKEKB is an upgrade from the previous collider KEKB.

The SuperKEKB collider is a B factory, meaning that its main goal is to look at CP violation through B mesons. The beams at SuperKEKB are targeted to mostly have $\sqrt{s} = 10.58$ GeV, which is the invariant mass of the $\Upsilon(4S)$ meson which mainly decays into $B\bar{B}$ pairs. The energy however can be tuned to different energies. In addition, an asymmetry between the beam energies is present in order to "boost" the particles produced. This plays a significant role for searching CP violation as this causes B meson pairs to travel further in the detector which makes a better time dependent measure of CP asymmetry. The centre of mass frame is boosted with respect to the laboratory system with a Lorentz factor of $\beta\gamma = 0.28$. Although the machine is mainly used for B physics, the clean environment from the lepton collision compared to hadronic collisions, and the high luminosity offering better precision, has allowed various other areas of particles physics to be explored.

The SuperKEKB collider has a high luminosity. The design instantaneous luminosity of SuperKEKB is $8 \times 10^{35}\,\mathrm{cm}^{-2}\mathrm{s}^{-1}$, which is 40 times higher than what KEKB had. This will aid the goal of reaching an integrated luminosity of $50\,\mathrm{ab}^{-1}$. The gain in luminosity is achieved mainly through two ways; decreasing the beam sizes at the interaction point (IP), and increasing the beam current [16]. In June 2020, SuperKEKB achieved a new instantaneous luminosity world record of $2.4 \times 10^{34}\,\mathrm{cm}^{-2}\mathrm{s}^{-1}$ [17].

The schematics of the SuperKEKB collider can be seen in figure 2.1. The electrons and positrons are produced and accelerated separately. The electrons are generated in the pre-injector, accelerated through the linear accelerator (LINAC), and sent to the high energy ring (HER) at 7 GeV. To create positrons, electrons are accelerated to impinge the tungsten target in the middle of the LINAC to irradiate positrons. These positrons are then

accelerated to 4 GeV and are injected into the low energy ring (LER).

The data taking and commissioning of the SuperKEKB collider was carried out through three main phases.

- Phase 1 (2016): Phase without collisions nor focus systems to study beam background. The Belle II detector was not installed and the BEAST II beam background detector was used instead. Studies such as low emittance optimization and the tuning of the feedback system were also performed [18].
- Phase 2 (2018): Phase with collisions running at low luminosity to ensure both the accelerator and the detector were working as expected. The vertex detector however was not installed at this stage [19].
- Phase 3 (2019): Phase with the full Belle II detector running at full luminosity.

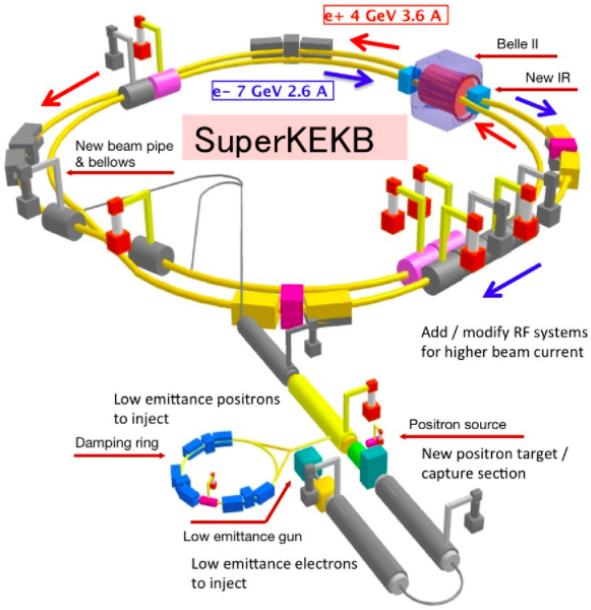

Figure 2.1: The SuperKEKB accelerator [20].

2.2 The Belle II detector

The Belle II detector is the only detector designated for the SuperKEKB collider, and it has been upgraded from the previous experiment Belle. The upgrade was to ensure good performance accompanying the increase of luminosity from the collider and coping with the substantial increase of background hits. Several sub-detectors were upgraded for Belle II. The installation of pixel detectors in the vertex detectors ensure better resolution, replacement of resistive plate chambers (RPC) by scintillators allows better reconstruction, better particle identification system means better separation between pions and kaons, and many more [21].

The detector is cylindrically symmetric around the beam pipe and is composed of many sub-detectors. The schematics of these sub-detectors can be seen in figure 2.2, and the cross sectional view can be seen in figure 2.3.

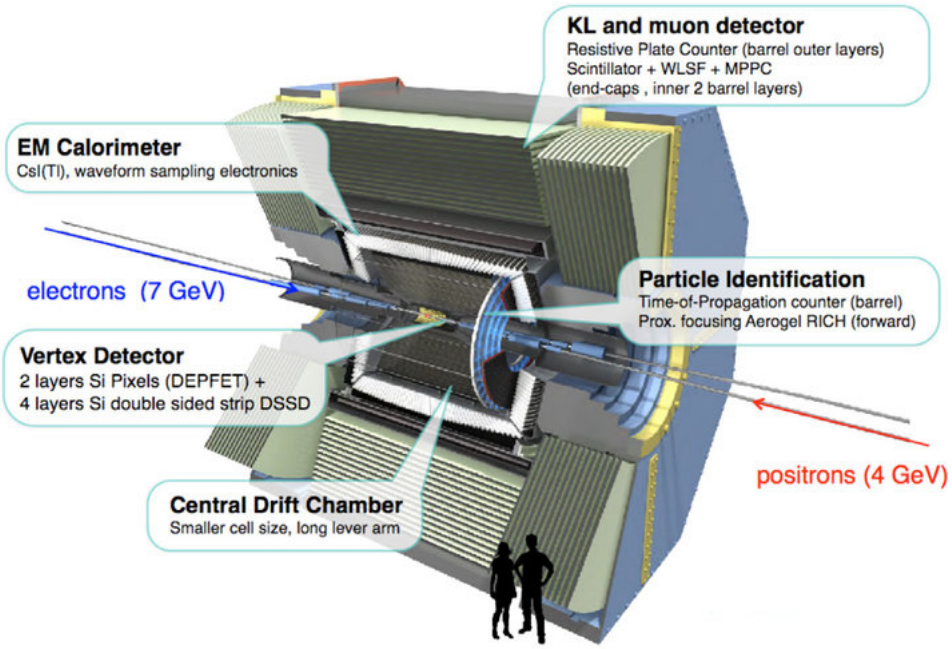

Figure 2.2: The Belle II Detector.

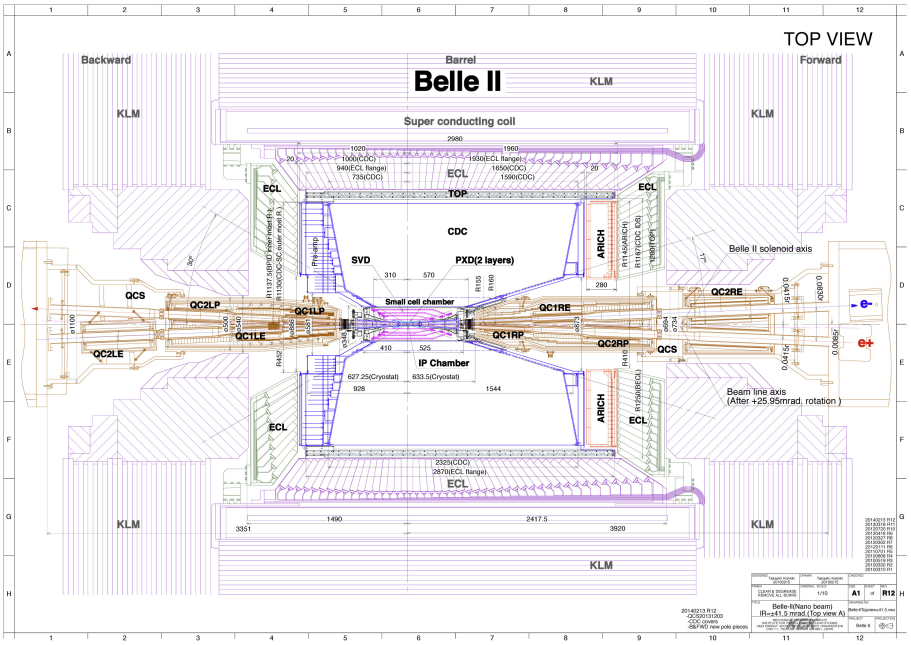

Figure 2.3: Cross sectional view of the Belle II detector [22].

A summary of the sub-detectors is below, in order of innermost to outermost from the beampipe:

- Vertex detector: The innermost sub-detector used for vertex detection and is directly on the beryllium beam pipe at the IP. It consists of the pixel detector (PXD) and the silicon vertex detector (SVD).
- Central drift chamber: This cylindrical wire chamber is the Belle II's main track reconstruction detector. It is filled with a 50:50 mixture of He and C_2H_6 gas [23].
- Particle identification system: This consists of the time of propagation (TOP) counter, which is a Cherenkov detector to locate the position and record the time of arrival of Cherenkov photons, and the aerogel ring-imaging Cherenkov (ARICH) detector, which is filled with aerogel using a Cherenkov radiator to identify charged particles [23].
- Electromagnetic calorimeter: The main detector used to detect photons and electrons through thallium-doped cesium iodide (CsI(Tl)) crystals. The scintillation light from particles is used to mainly detect the energy, timing, and position of the particles.

- Superconducting magnet: The NbTi/Cu magnet generates a 1.5 T magnetic field which causes charged particles to curve in order to measure their momentum.

- K_L muon detector: Located at the very outer layer of the detector, the K_L muon detector consists of iron plates and active detector elements located outside the superconducting solenoid [23]. Its main purpose is to detect K_L and muon particles, as they are highly penetrative particles, going through the multilayered detector without much interaction.

2.2.1 Vertex detector

The vertex detector is a combination of two detectors; the PXD and the SVD. In order to account for the high background rate, two layers of pixel detectors are used instead of silicon strip detectors as it has finer segmentation and lower occupancy, which is an upgrade from Belle. The vertex detector covers between 17° and 150° in the polar direction. The asymmetry in the range is attributed to events mainly being boosted in the forward direction.

The PXD consists of two layers of pixelated sensors using the depleted field effect transistor (DEPFET) technology. The first layer has 8 ladders and the second layer has 12 ladders with a total of 40 DEPFET sensors on the ladders. The layers of the PXD are located at 14 mm and 22 mm from the IP. The purpose of the DEPFET technology is to execute detection and amplification at the same time. The DEPFET is a monolithic sensor, and its design makes the pixels thinner, causing less usage of material (0.21% of radiation length). This is crucial to suppress multiple scattering. Furthermore, less material also means less power consumption, where no active cooling is required for the PXD. Belle II is the first particle physics experiment to implement a DEPFET based pixel detector [24].

The SVD consists of four layers of double-sided silicon strip detectors. The layers labelled 3, 4, 5, and 6, are located at 38 mm, 80 mm, 115 mm, and 140 mm respectively from the IP. Three different sensors with different shapes are used for detection. In order to account for the increase in luminosity, it will use a better readout chip called APV25 with a short shaping time of 50 ns. Newly implemented features also include the Origami chip-on-sensor. This system allows all ladders to have only one combined cooling system by aligning all of the readout chips on one side, taking advantage of the windmill structure of the ladders.

2.2.2 Central drift chamber (CDC)

The central drift chamber (CDC) is the main tracking device for Belle II, and it serves three main purposes [25]. Firstly, it allows precise measurements of the momenta of the charged particles and track reconstruction. Secondly, the energy loss measurement within the CDC provides particle identification. Lastly, it allows trigger signals for charged particles. Although the overall structure of the CDC follows the Belle CDC, there has been changes made to the different configurations of the material. The readout electronics has also been updated in order to handle a higher trigger rate [25].

The CDC is a cylindrical wire drift chamber, 2.3 m in length and 2.2 m in diameter. The radius of the inner cylinder is at 160 mm and the radius of the outer cylinder is at 1130 mm. The innermost radius is significantly larger than Belle to account for higher background rates. The outer radius also extends at a larger radius compared to Belle as the particle identification system was made to be thinner. The CDC's main structure is supported by two thin carbon-fiber reinforced plastic cylinder with thickness of 0.4 mm and 5 mm for the inner and outer cylinders respectively, and two aluminum endplates with 10 mm thickness, located between the CDC and the electromagnetic calorimeter (ECL). The gas is filled with 50% Helium (He) and 50% ethane (C_2H_6). The CDC has 14,336 cells arranged in 9 super layers, with a total of 56 layers. Each cell has a sense wire made from tungsten, which is covered by 8 field wires made from aluminum. The mechanism of the CDC is such that when a charged particles passes the CDC, its ionization through gas produces electrons. These electrons are then accelerated from the field wire by the electric field. The charges of the electrons are then collected by the sense wires, which the amount of signal and timing are stored.

The read-out electronics allows the CDC to be connected to the detector, the Belle II data acquisition (DAQ) system, and the level 1 trigger system. The read-out system, located at the back-end of the detector, consists of an analog and digital processor. The analog part works to amplify signal, shape the waveform, and discriminate signal. The analog data is then converted to digitized data which then functions to cancel trigger delays, reduce data size, and transfer data to the trigger system and the DAQ [26].

The spatial resolution for the CDC is roughly 100 µm, and the precision of the dE/dx measurement of particles with incident angle of 90° is around 12% [27].

2.2.3 Particle identification system (PID)

Particle identification is crucial for B factories, where a good π and K identification from B decays is necessary for precision measurement in CP violation [28]. There are two parts of the particle identification (PID) system; the TOP counter in the central barrel region, and the ARICH in the forward endcap.

The TOP detector consists of 16 modules located around the IP in the barrel region. Each module has four parts; two fused silica bars each with dimension $(1250 \times 450 \times 20)$ mm^3, a mirror at the forward end of the bar, and a prism at the end of the bar. The fused silica bars have refractive index of $n = 1.44$ at 405 nm and act as a Cherenkov radiator [29]. The high refractive index allows part of the Cherenkov radiation to be completely trapped by total reflection where the mirror also reflects the light backwards. The radiation is transmitted to the prism which then couples the bar to the micro-channel-plate-photomultiplier tube (MCP-PMT). The MCP-PMT allows precise measurements of the time of the particle through two ways; the time of flight of the particle to the TOP from the IP, and the time of propagation of the Cherenkov light inside the module, which is dependent on the Cherenkov angle. The TOP is part of the PID system as it extracts the distribution of the time of arrival of the photons and fits the probability distribution function for six particle hypotheses; e, μ, π, K, p, d [30].

The ARICH detector also exploits Cherenkov radiation to discriminate mainly π and K. It consists of three components; aerogel tiles used as a radiator, position sensitive photon detectors, and a readout system [31]. In addition, there is an expansion volume between the aerogel and the photon detector in order to provide Cherenkov photons to create rings onto the detector surface. In building the ARICH, there is a trade-off between the two most important variables; the number of photons detected (N_γ) and the resolution of the Cherenkov angle (σ_θ) [25]. A longer radiator ensures an increase in the number of photons detected but degrades the angular resolution of the Cherenkov angle. In order to avoid this issue, the aerogel tiles were made with two layers of different refractive indices ($n_1 = 1.046, n_2 = 1.056$), which improved the resolution from $\sigma_\theta = 20.7$ mrad to $\sigma_\theta = 14.3$ mrad [25].

2.2.4 Electromagnetic calorimeter (ECL)

The ECL is the main sub-detector for photons, hence a detailed description is necessary as the analysis for dark photon is heavily reliant on this instrument. The ECL serves many roles within the experiment; it measures the energy and position of the photons, measures electrons which are used for kaon detection together with the K_L muon detector (KLM), it generates triggers for photons, and lastly is also used to record the luminosity of the beam.

The two key aspects of the ECL are material and geometry. The scintillating material is crucial for maximising output as well as minimising the production cost. Geometry is important to understand the structure of the ECL and create a visual representation of how the particles are travelling from the IP. The crystals have been inherited from Belle, however the readout electronics has been updated in order to account for the increase in luminosity.

When choosing the scintillating material and the design of the ECL, there are two main things to consider; radiation length and Moliere radius. Radiation length X_0 is defined by the length which a high energy particle loses all but $1/e$ of its energy. Ideally the particle should be contained within the ECL, hence the short radiation length. The Moliere radius R_m, defined by equation 2.1, is the value of which 90% of the energy of an electromagnetic (EM) shower is contained in the cylinder of radius R_m. E_c represents the critical energy, when the collision loss rate becomes the same as the bremsstrahlung rate. For Belle II, CsI(Tl) was used for the material.

$$R_m = \frac{21\text{MeV}}{E_c} \times X_0 \ [\text{g/cm}^2] \tag{2.1}$$

CsI(Tl) Crystals

The main component of the ECL, which are the crystals, are made of CsI(Tl). The material has a property of $X_0 = 1.860\,\text{cm}$ and $R_m = 3.53\,\text{cm}$ [32]. It is known as one of the brightest scintillators, which has a light output of 54 photons per keV [32]. The doping of thallium causes the photo emission spectrum to be shifted at $\sim 550\,\text{nm}$, which is the ideal wavelength for the photo-diode readout. The difference between a pure CsI crystal and a doped crystal is that although the pure crystal has faster decay times, it has less brightness and less favorable emission spectrum. There have been on-going talks about switching to pure CsI crystals for Belle II, however no progress has been made so far. The crystal configuration has not been changed from

the previous Belle experiment. The ECL comprises 8736 CsI(Tl) crystals, weighing 43 tons [33]. Each crystal is arranged to point to the IP with a small tilt of angle $\sim 1.3^\circ$ in the theta and phi direction in barrel and an angle of $\sim 1.5^\circ$ and $\sim 4^\circ$ in the theta direction in the forward and backward endcaps. The geometry overview of the ECL can be seen in figure 2.4. Each crystal has a unique cell ID starting from 0 to 8736, which is based on the theta ID and phi ID. Crystals that are aligned in the same theta angle all have the same theta ID, which starts from 0 when the outer edge of the crystal is at 12.42°, and ends at 68 which the outer edge of the crystal is at 154.69°. Crystals are also assigned phi IDs, with 0 starting roughly at 3.8°. Depending on the region, the number of phi IDs may differ. In the barrel region, each theta ID has phi IDs ranging from 0 to 143, covering the entire azimuthal angle. A cross sectional view of the crystals with theta IDs can be seen in figure 2.5. The crystals cover about 90% of the solid angle in the center of mass system [34]. There are three main gaps in the ECL; a 1.5 mm gap directly above the IP between theta ID 41 and 42 which can be seen in figure 2.5 with the vertical line, the gap between the endcaps and barrel between theta ID 12 and 13 and also between theta ID 58 and 59, and the gaps between the individual crystals. The crystals have a quadrangular prism shape, with the two ends having different surface areas. The individual crystal geometry with a schematic drawing of the photon shower is shown in Figure 2.6. For the barrel, the crystals are 55 mm by 55 mm for the front face and 65 mm by 65 mm for the rare face, whereas for the end cap parts, they are in a range of 44.5 mm by 44.5 mm to 70.8 mm by 70.8 mm for the front face, and 54 mm by 54 mm to 82 mm by 82 mm for the rare face. Each crystal has length of 300 mm, which corresponds to $16.1X_0$ [34].

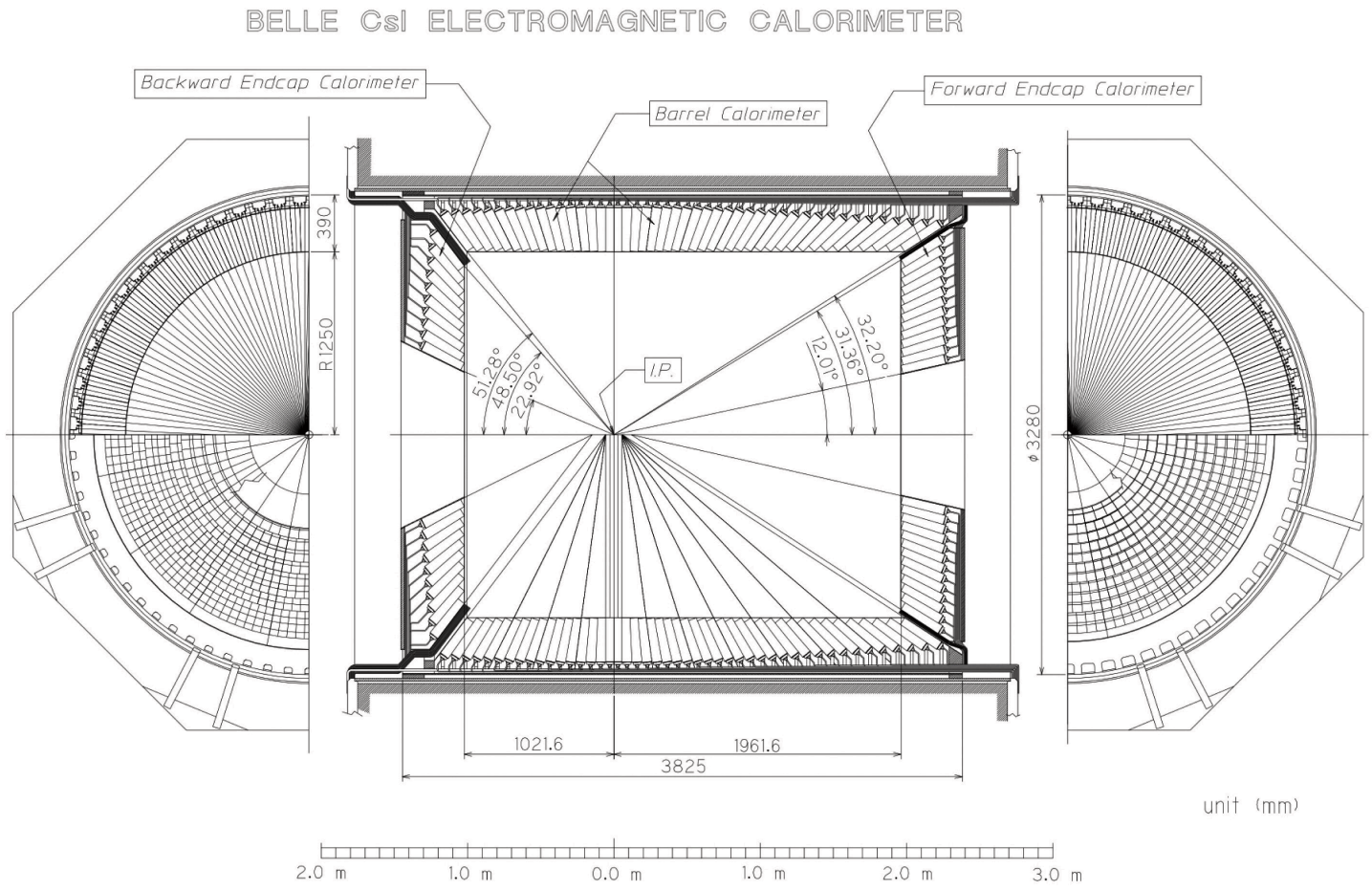

Figure 2.4: Geometry overview of ECL at Belle II [34].

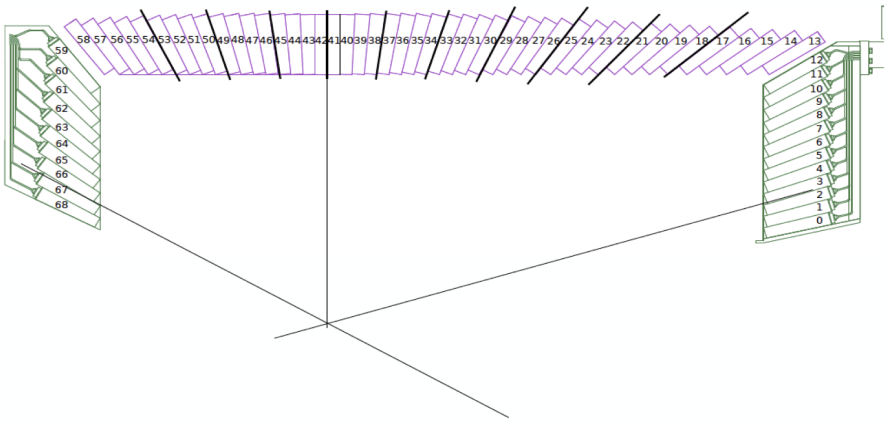

Figure 2.5: Cross sectional view of the ECL with theta IDs.

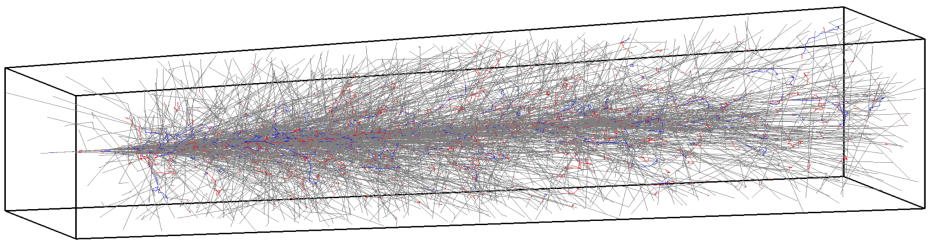

Figure 2.6: Schematic drawing of a cascade of photon showers within one crystal of the ECL.

Electronics

As seen in figure 2.7, each crystal is wrapped with a layer of 200 µm thick Gore-Tex porous teflon and covered by the 50 µm thick aluminized polyethylene [33]. In order to collect the scintillation light, there are two $10 \times 20\,\mathrm{mm}^2$ Hamamatsu S2744-08 photodiodes glued to the rear surface of the crystal via an intervening 1 mm thick acrylite plate [33]. Signals from the photodiode are fed to a charge sensitive amplifier mounted on the crystal, and the pulses are collected onto a digitizer [34]. The signals are sampled in 16 points, and a fitting is applied to the signal shape using a predefined function. The upgraded readout electronics from Belle has allowed the pulse shaping time to shorten from 1.0 µs to 0.5 µs [34].

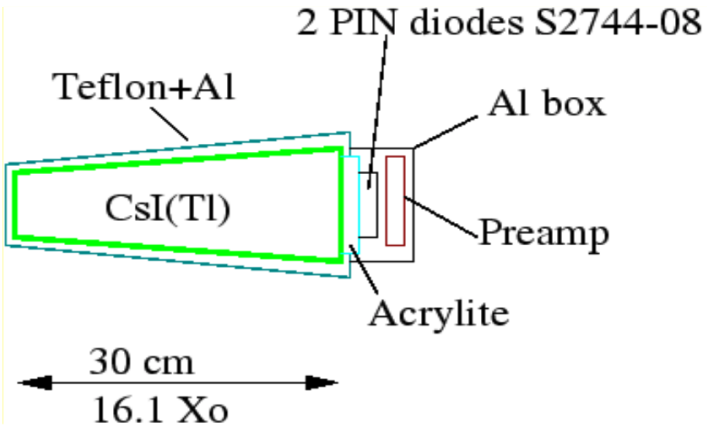

Figure 2.7: Schematic drawing of the electronics wrapping the crystal of the ECL.

However, even with the upgraded electronics, there is still background noise which cannot be suppressed. The most serious effect is due to the pile up noise caused by the soft background photons with average energy of $E < 1\,\text{MeV}$ [33]. The calculated pile up noise at the Belle II ECL ranges from 3 to 8 MeV, even with the upgrade [33]. Furthermore, the average output signal of the crystals with cosmic rays is measured to be about 5000 photoelectrons per 1 MeV.

The energy resolution of the calorimeter σ_E measured from a prototype test is given by:

$$\frac{\sigma_E}{E} = \sqrt{\left(\frac{0.066\%}{E}\right)^2 + \left(\frac{0.81\%}{\sqrt[4]{E}}\right)^2 + (1.34\%)^2} \tag{2.2}$$

where the energy E is given in GeV. σ_E/E was 1.7% for $E = 5\,\text{GeV}$ [33].

ECL Cluster

A particle in the ECL is identified through a cluster. When a particle emits an EM shower as it traverses through the crystal, the energy deposit may spread to more than 1 crystal. The ECL tries to group the crystals together to form a cluster associated with a particle, and take out additional noise unrelated to the event. An algorithm takes the digitized numbers from the photo-diode and connects the crystals to form a cluster. A simplified version of the algorithm is listed below [35]. The cluster contains information such

as the EM shower shape of the particle, the position in the ECL, and the total energy deposit.

1. Find crystals which have energy deposit more than 10 MeV.
2. If there are neighboring crystals which have more than 0.5 MeV, attach it to the original crystal to form a cluster.
3. If there are neighboring clusters which are overlapping, the clusters are merged.

After all of the crystals are connected, further work is performed. A cluster can be spread over 5×5 crystals, although a cluster may only have 1 crystal. At Belle II, the local maximum of the particle shower is considered to be the crystal which has more than 10 MeV of energy deposit and has the highest energy among its neighbouring crystals. When there is more than 1 local maximum crystal per cluster, the cluster is split into the number of local maximums by weighing the crystal's energy. Belle II is currently testing machine learning approaches for better position reconstruction [35].

The reconstructed energy in the ECL is the energy deposited in the crystals with a correction. The correction is applied after each cluster has 1 local maximum. The correction is to account for two things; leakage energy and beam background. There is always a longitudinal and transverse leakage of energy from the crystals, represented by a low tail of the energy distribution of a particle as they will never deposit its full energy. Corrections are necessary to account for this effect. In addition, the energy distribution has a high tail for low energy clusters. This is because beam background particles, unrelated to the event, are added to the cluster which then overestimate the cluster's total energy. Energy correction is crucial to take this into account as well. After the corrections, a cluster is finalised and can be used to identify the different types of particles and measure its energy and position.

Shower shapes are used to identify particles. For example, photons and electrons have radially symmetric showers whereas pions have an asymmetric lateral spread due to hadronic interactions. Muons only deposit their energy in 1 or 2 crystals as they are minimum ionizing particles and hardly interact with the ECL. Further progress of particle identification using shower shapes has been made with the use of machine learning at Belle II.

2.2.5 Superconducting magnets

Between the KLM and ECL, there is the superconducting solenoid, made of NbTi/Cu which produces a magnetic field of 1.5 T parallel to the beam, and covers a cylindrical volume of 3.4 m in diameter and 4.4 m in length [36]. The iron yolk structure of the detector is not only an absorber for the KLM, but also creates a return path for the solenoid's magnetic flux. Its main purpose is to create a curved path in the azimuthal angle for charged particles traversing through the detector. A cryogenic system is used for cooling. Although mainly homogeneous, there are inconsistencies in the magnetic field due to edge effects and the presence of the final focus system magnets of the SuperKEKB [27].

2.2.6 K_L muon detector (KLM)

The KLM lays outside the superconducting solenoid and is made of alternating iron plates and active material detectors. Its main purpose is to detect and identify muons and kaons which are long lived and penetrate through most of the sub-detectors. The reconstruction of these particles is done by combining the KLM information with the ECL.

As seen in figure 2.8, the KLM is made of three parts; forward endcap, barrel, and backward endcap. The endcaps together cover a polar angular range of $20° < \theta < 155°$, with barrel covering $45° < \theta < 125°$. The forward endcap, barrel, and backward endcap each have 15, 14, and 12 detector layers respectively, with alternating iron plates for all regions. The iron plates are 4.7 cm thick which is roughly 3.9 interaction lengths, in addition to the 0.8 interactions lengths from the ECL [25]. The endcap regions and the two innermost layers in barrel closest to ECL are made with two orthogonal layers of scintillator strips which are read out with silicon photomultipliers (SiPM). The other layers are RPC, which is a proportional gas chamber. The SiPM are to account for the long dead time of the RPCs when there is a discharge. The KLM has a large gap in the barrel near the backward endcap which can be seen in figure 2.8, due to the chimney structure where cables are located for hardware.

There are multiple steps to identify a muon with the KLM. The muon reconstruction starts from the CDC tracks, where each track is extrapolated to the KLM with a pion hypothesis. If a track crosses at least one RPC layer, it is considered to be within KLM acceptance. KLM hits that are within the extrapolation region from the CDC are matched, and the outermost layer crossed by the extrapolated track becomes the predicted range of the

hit, while the actual range is the outermost layer of the KLM hit. The two different ranges are compared, and if there is an agreement, the extrapolation starts over again, this time with a muon hypothesis. Similar to the previous steps, a likelihood ratio is performed. The ratio uses the predicted and actual range as well as the goodness of fit of the transverse deviations of the associated hits from the extrapolated tracks. The muon detection efficiency plateaus at 89% for above 1 GeV/c. The hadron fake rate is 1.3% where hadrons such as pions have not decayed and look similar to a muon [25].

The reconstruction works differently for K_L particles. KLM clusters combine hits in the KLM which are within 5° opening angle of one another, regardless of layer number. If there is an ECL cluster within 15° opening angle to the KLM cluster, the two clusters are associated. After the association, the information is passed onto a boosted decision tree (BDT) in order to classify the cluster as a K_L particle. The detection efficiency for K_L particles plateau at 80% at 3 GeV/c [25].

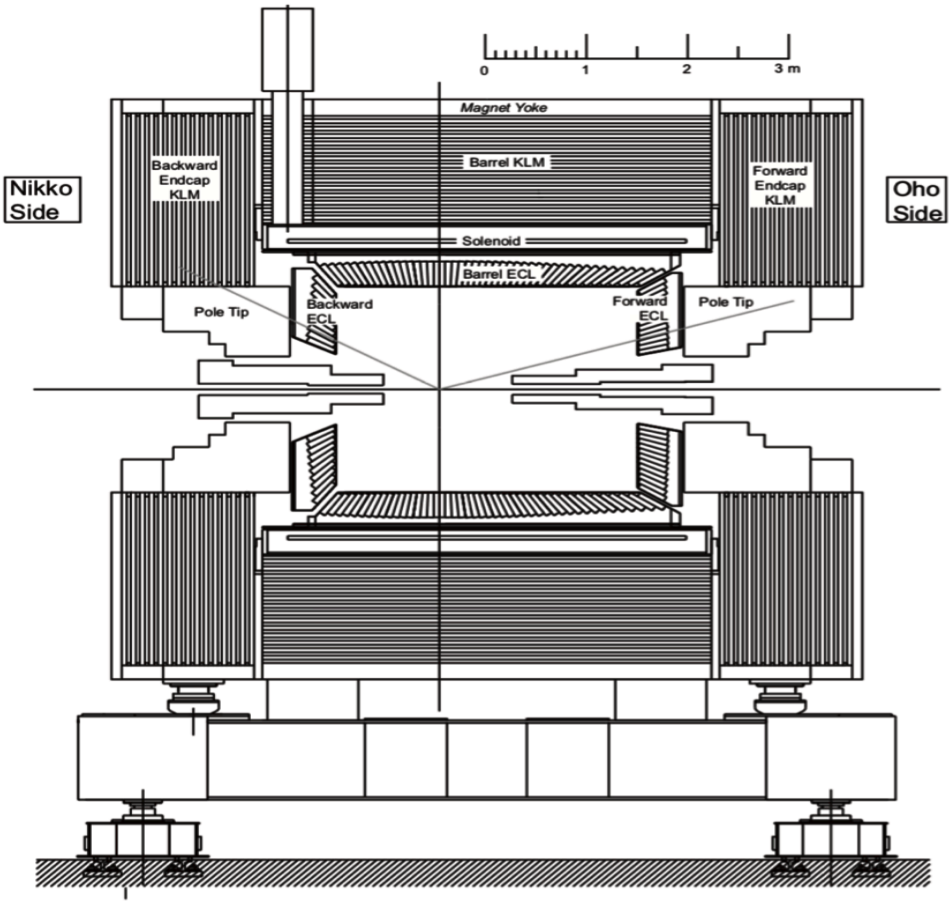

Figure 2.8: Geometry overview of the KLM at Belle II.

2.3 Trigger

Belle II uses the trigger system for minimising background events and selecting interesting physics events worth storing. The main events which the trigger eliminates are $e^+e^- \to e^+e^-$ (Bhabha event) and $e^+e^- \to \gamma\gamma$ which both have high cross section. In order to maintain high efficiency for $B\bar{B}$ events, the maximum average trigger rate has to be kept or below at 30 kHz, with a fixed latency of 5 µs, and with a timing precision of less than 10 ns. The minimum separation time between two events also has to be kept at 200 ns [37]. The trigger system is a combination of the hardware based level 1 (L1) trigger, and the software based high level trigger (HLT).

The L1 trigger uses four systems to make a trigger decision; the front-end readout system, the four sub-trigger systems, the general reconstruction logic (GRL), and finally the general decision logic (GDL).

The front-end readout system continuously provides information to the four sub-trigger systems which are based on the CDC, ECL, TOP, and KLM data. Each of the sub-detector trigger summarises its own trigger information using data from its own system. This data is then relayed to the GRL where the information is combined and low level reconstruction is executed. The GDL then further uses the information in the final stage of the trigger to calibrate the decision. If the L1 trigger returns positive, the trigger signal relays back to the readout system using the trigger and timing distribution system. The trigger components have a field-programmable gate array which was not used in Belle in order to provide a configurable system rather than a hard-wired system. Although there are four sub-trigger systems, the main sub-detectors used are the CDC and ECL. The CDC trigger uses charged tracks and applies both a 3D and 2D reconstruction. The 3D tracking takes into account the z-coordinate along the beampipe, which rejects background events with displaced vertex such as from the Touschek effect. In order to perform this reconstruction with low latency, neural network techniques are being applied [38]. The ECL trigger focuses on the total energy released in the calorimeter per event, as well as the number of isolated clusters.

The HLT trigger is used to further reduce the data that can be stored, at an event rate of 10 kHz [39]. HLT trigger uses the offline reconstruction from the full output of all the sub-detectors except the PXD. With this information, a trigger is applied.

Chapter 3

Search for dark photons

3.1 Analysis overview

This chapter will describe the search for dark photons at Belle II. The search is for an event signature of $e^+e^- \to \gamma A'; A' \to \chi\chi$, where the dark photon A' kinetically mixes with a SM photon, and there is a single recoil photon being produced. The dark photon then decays invisibly to two dark matter candidates χ. In the final state, the only particle visible in the detector is the single recoil photon. This is under the assumption that A' is not the lightest dark sector particle, and if so, it will decay into a SM particle. The Feynman diagram of this event is presented in figure 3.1. Similar searches with the same signature are conducted at the BaBar experiment [40] and NA64 experiment [41].

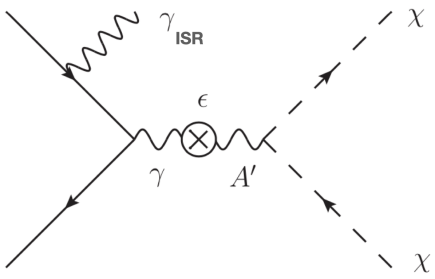

Figure 3.1: Feynman diagram of the invisibly decaying dark photon event.

The goal for this analysis in the end is to conduct a "bump" hunt on the invariant mass of the dark photon, which is measured by the single photon energy using equation 3.1. $m_{A'}$ represents the dark photon mass, $E^*_{\gamma\text{ISR}}$ is the center of mass (CoM) energy of the single recoil photon, and E^*_{beam} is the CoM energy of the beam.

$$m^2_{A'} = 4E^*_{\text{beam}}(E^*_{\text{beam}} - E^*_{\gamma\text{ISR}}) \tag{3.1}$$

The sensitivity of the dark photon at Belle II with $20\,\mathrm{fb}^{-1}$ of data is shown in figure 3.2, as a function of the coupling strength ϵ and the dark photon mass $m_{A'}$.

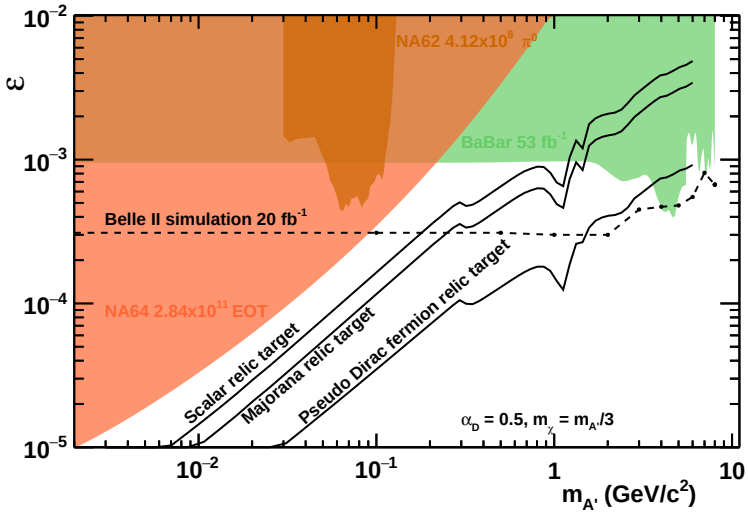

Figure 3.2: Sensitivity and constraints of the dark photon at Belle II in the coupling strength ϵ and mass parameter space $m_{A'}$ [15]. The sensitivity for the experiments is for the next 5 years. The black lines indicate the thermal targets for different dark matter decays.

This search requires a trigger sensitive to low energy single photons, which was not available at Belle [23]. Currently, there are two L1 triggers; lml6 and lml13, that affect the single photon studies, listed below [42].

1. lml6: 1 cluster with $E^* > 1\,\mathrm{GeV}$ with $4 \leq \theta_{ID} \leq 15$, corresponding to $32.2° < \theta < 128.7°$ in the full ECL barrel region, and no other clusters with $E > 300\,\mathrm{MeV}$ anywhere in the detector.

2. lml13: 1 cluster with $E^* > 0.5\,\mathrm{GeV}$ with $6 \leq \theta_{ID} \leq 11$, corresponding to $44.2° < \theta < 94.8°$ in the full ECL barrel region, and no other clusters with $E > 300\,\mathrm{MeV}$ anywhere in the detector.

In order to measure the trigger efficiency, a radiative muon pair control sample of $e^+e^- \to \mu\mu\gamma$ was used. The efficiency for both L1 and HLT was 99%. The efficiency using the 0.5 GeV single photon threshold is shown in figure 3.3. The drop in efficiency for both triggers at the 0.5 GeV threshold is due to the calibration and clustering resolution.

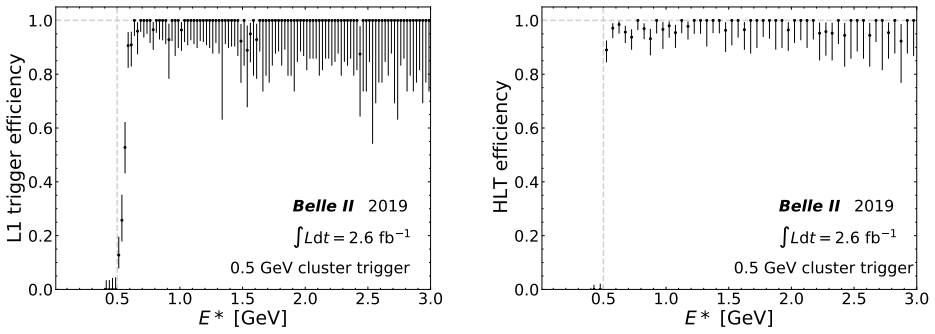

(a) **(b)**

Figure 3.3: **(a)** Trigger efficiency of the L1 trigger for 0.5 GeV single photon events using a radiative muon control sample as a function of CoM energy of the photon. **(b)** Trigger efficiency of the HLT trigger for 0.5 GeV single photon events using a radiative muon control sample as a function of CoM energy of the photon.

The first step of this search was to quantify the expected background before un-blinding data. The dark photon events which needs to be kept are called signal events, as opposed to background events which are SM physics processes which look similar to the signal event and needs to be reduced. The background analysis is split into roughly three main regions depending on the A' mass, as the dominant background processes are different for each region. Figure 3.4 shows the different backgrounds depending on the CoM energy of the photon which acts as a single photon. The different backgrounds are listed below depending on the dark photon mass region, with E^* representing the CoM energy of the single photon.

- High $m_{A'}$, Low E^*: Main background is $e^+e^- \to e^+e^-\gamma$, where both e^+e^- are out of the tracking acceptance.
- Middle $m_{A'}$, Middle E^*: Main background is $e^+e^- \to \gamma\gamma\gamma$, where 2 γs are not reconstructed.
- Low $m_{A'}$, High E^*: Main background is $e^+e^- \to \gamma\gamma$, where 1 γ is not reconstructed.

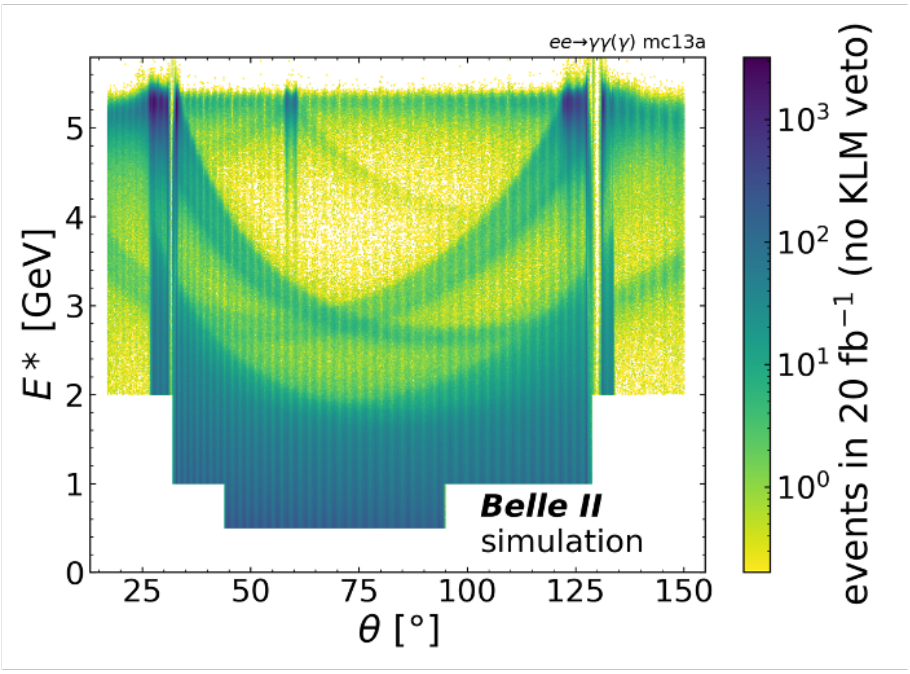

Figure 3.4: CoM energy against lab frame theta of a photon from MC background events; $e^+e^- \to e^+e^-\gamma$, $e^+e^- \to \gamma\gamma\gamma$, and $e^+e^- \to \gamma\gamma$.

The analysis presented in this report will be for the last region, with low $m_{A'}$ having a range from $0.01\,\mathrm{GeV/c^2}$ to roughly $0.5\,\mathrm{GeV/c^2}$. In this case, the E^* of the single photon will become roughly beam energy of 5.29 GeV for Belle II. The dominant background, as written above, becomes $e^+e^- \to \gamma\gamma$. This background event looks like a dark photon event when one of the photons is missed by the detector, which happens mainly due to the gaps between the sub-detectors of the ECL and KLM. The main gaps in the ECL are the 1.5 mm gap directly above the IP between theta ID 41 and 42, the gap between the endcaps and barrel, and gaps between the individual crystals. For KLM, there is a large gap due to the chimney structure where cables are located for hardware. Without any polar angular cuts on the photons and with a minimum photon energy of 0.01 GeV, this background event has a very high cross section of $\sigma_{\gamma\gamma} = 25.2\,\mathrm{nb}$ [23]. When an additional polar angular cut of $10° < \theta^* < 170°$ is added to the selection criteria, the cross section drops to 4.99 ± 0.05 nb [23], which is roughly the detector acceptance for Belle II.

In order to study this background, the goal was to answer two main questions:

1. What is the efficiency of both sub-detectors? What are the likelihoods that both the ECL and KLM miss a photon?

2. How are the efficiencies different between Monte Carlo (MC) and data? Do both events follow the same pattern?

Multiple types of events were studied to answer these questions. For MC events, there are two main event types; background and signal events. For background events, $e^+e^- \to \gamma\gamma$ and $e^+e^- \to e^+e^-$ (Bhabha) events were used, and for signal, the $e^+e^- \to \gamma A'; A' \to \chi\chi$ event was used with different dark photon masses. All MC events were generated using an event generator tool. For background events, BABAYAGA.NLO [43] was used. The event generator provides a four vector of the particles which is then processed by GEANT4, a toolkit used for simulation [44]. GEANT4 simulates the passage of the particles through the detector, which includes the detector response. Similarly, signal events were generated using MadGraph5 [45]. For all MC events, after the GEANT4 detector simulation, beam background events were also manually added. Finally, the events were then reconstructed using basf2 [46], the Belle II software, where a python script called a steering file produced ntuple files. The reconstructed values in the ntuple files will not be the same as the generated values, as the detector is limited by its resolution and efficiency. The ntuple files store information of the particles per event which are then analysed offline using python.

Data-sets taken at different periods were also studied. The run down of the different data-sets used are presented in table 3.1 for MC events, and table 3.2 for data. Bucket and Proc(Processing) are two different types of processing labels. The Bucket label is for prompt productions, where calibrations are done immediately after the data is collected, while the Proc label is for official productions, which includes updates and improvements. The number for Proc represents the different versions of releases. For MC events, run dependent events were generated in a similar setting as the corresponding data, with the same beam background overlaid from data as well as the same sub-detector efficiencies. The luminosity is also the same. Run independent events are generated with the default geometry. The different productions were explored as some of the detector responses have been improved throughout data taking. In addition, calibration is better for processed events, which would yield a more accurate result.

Name	Luminosity (fb^{-1})	Type
MC13a [47]	100.0 ± 0.1	Run independent
MC13b Proc10 Exp8	4.586 ± 0.002	Run dependent
MC13b Proc11 Exp10	3.685 ± 0.002	Run dependent
MC13b Buckets 9, 10, 11, 13, 14, 15 Exp12	54.031 ± 0.005	Run dependent

Table 3.1: Summary of type of MC files used.

Name	Luminosity (fb^{-1})	Duration
Proc11 Exp7 [48]	0.4247 ± 0.0007	Mar 11, 2019 - May 9, 2019
Proc10 Exp8 [49]	4.586 ± 0.002	May 9, 2019 - Jun 26, 2019
Proc11 Exp8 [48]	4.586 ± 0.002	May 9, 2019 - Jun 26, 2019
Bucket8 Exp10 [50]	3.685 ± 0.002	Sep 24, 2019 - Dec 13, 2019
Proc11 Exp10 [48]	3.685 ± 0.002	Sep 24, 2019 - Dec 13, 2019
Buckets 9, 10, 11, 13, 14, 15 Exp12 [51]	54.031 ± 0.005	Feb 17, 2020 - Jul 7, 2020

Table 3.2: Summary of type of data files used.

3.2 Efficiency studies

In order to understand the efficiency and geometry of the ECL and KLM, the efficiency was measured as a function of the theta ID of the probe photon using the tag and probe method for different leakage energies. The tag and probe method is when there are two particles; the tag is for a good photon with high energy, and the probe is for the other photon pair. The probe photon is analysed closely. The definition of a good photon in this case was when it had an energy of above $E^* > 4.5\,\text{GeV}$. If both photons have $E^* > 4.5\,\text{GeV}$, then each of the photons are tag and probe to one another. Hence an event can have two tags and two probe photons at the same time, meaning that the number of tag and probe photons do not represent the number of events.

The leakage energy is defined by equation 3.2, where the difference between the theoretically expected CoM frame value of 5.29 GeV and the actual CoM energy calibrated by the ECL is boosted to the lab frame energy. 5.29 GeV was used as the generated energy for MC events.

$$E_{\text{leak}} = (5.29 - E^*) \times (E/E^*) \tag{3.2}$$

If E_{leak} is above 0 eV, then this means that some of the photon's energy has leaked out from the ECL crystal. The geometry of the crystals are made to ensure that high energy photons deposit its full energy within the crystal, however there are cases where there is high leakage. Most of these cases come from when a photon goes through the material gaps in the detector, and the energy escapes without being fully deposited in the calorimeter. The gaps come from the structure of the detector, which cannot be modified. Photons which have particularly high leakage of $E_{\text{leak}} > 2.8\,\text{GeV}$ are labelled as high leakage photons.

The criteria for choosing an $e^+e^- \to \gamma\gamma$ event was as follows, where these events were stored in the ntuple file:

- Use the 2 most energetic photons per event
- 1 photon must have CoM energy between $4.5\,\text{GeV} < E^* < 7.0\,\text{GeV}$
- 1 photon must have CoM energy between $0.1\,\text{GeV} < E^* < 7.0\,\text{GeV}$
- No charged tracks with $p_t > 0.2\,\text{GeV/c}$, $|z0| < 10.0\,\text{cm}$, $|d0| < 2.0\,\text{cm}$, and number of CDC hits > 0
- $\Delta\phi^* > 178^\circ$

- $178^\circ < \sum \theta^* < 182^\circ$

p_t is the transverse momentum of the particle, while $d0$ represents the distance to the interaction point in the $r\phi$ plane, and $z0$ is the distance of the z coordinate along the beampipe. $\Delta\phi^*$ is CoM azimuthal angular difference between the two photons, while the $\sum \theta^*$ is the CoM polar angular sum of the two photons. In addition to these cuts, a further cut of probe being in theta ID 14 to 57 was applied to insure there were no photons in the endcap and barrel gaps, which were the main causes of highly leaking photons. By applying the cuts above and attempting the tag and probe method, the cross section was reduced to 1.03 ± 0.01 nb.

The probe photons were split into 5 different regions depending on its leakage energy:

1. $E_{\text{leak}} < 0.35\,\text{GeV}$
2. $0.35\,\text{GeV} \leq E_{\text{leak}} < 0.70\,\text{GeV}$
3. $0.70\,\text{GeV} \leq E_{\text{leak}} < 1.40\,\text{GeV}$
4. $1.40\,\text{GeV} \leq E_{\text{leak}} < 2.80\,\text{GeV}$
5. $E_{\text{leak}} \geq 2.8\,\text{GeV}$

Figure 3.5 shows the number of probe photons found per crystal depending on the leakage energy. The comparison between figure 3.5a and figure 3.5e shows how the number of photons drop with the increase in leakage energy. Furthermore, mapping the positions of the photons allow better understanding of the ECL geometry. The dark band in figure 3.5e at theta ID 41 and 42 represents the 1.5 mm gap directly above the IP and is the main source of high leakage photons. The rims seen at the edge of theta ID 57 in figure 3.5a also signifies a drop in efficiency, which happens when the tag photon is at the forward endcap region. The endcaps have less efficiency compared to the barrel region, hence the tag is missed and the event does not get stored.

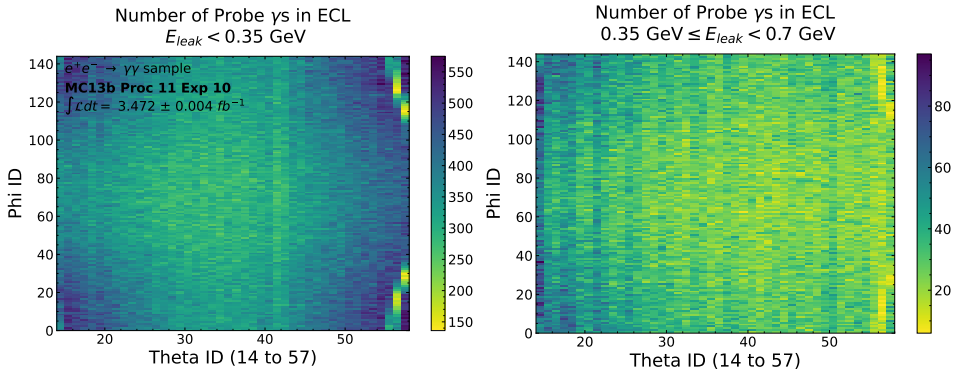

(a) $E_{\text{leak}} < 0.35\,\text{GeV}$

(b) $0.35\,\text{GeV} \leq E_{\text{leak}} < 0.7\,\text{GeV}$

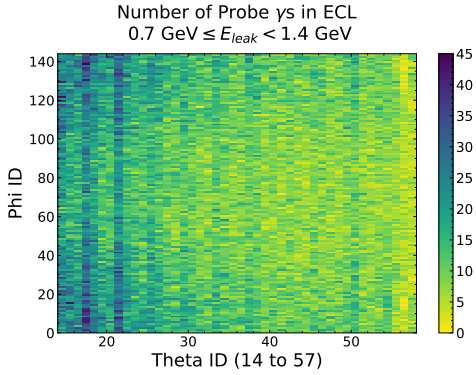

(c) $0.7\,\text{GeV} \leq E_{\text{leak}} < 1.4\,\text{GeV}$

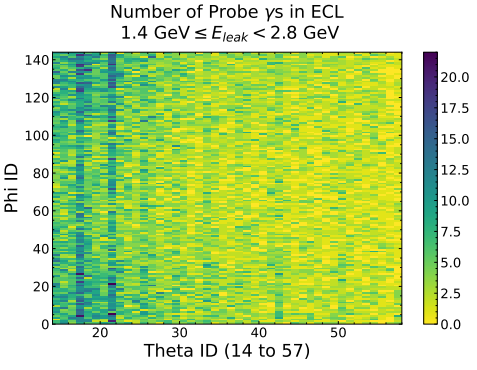

(d) $1.4\,\text{GeV} \leq E_{\text{leak}} < 2.8\,\text{GeV}$

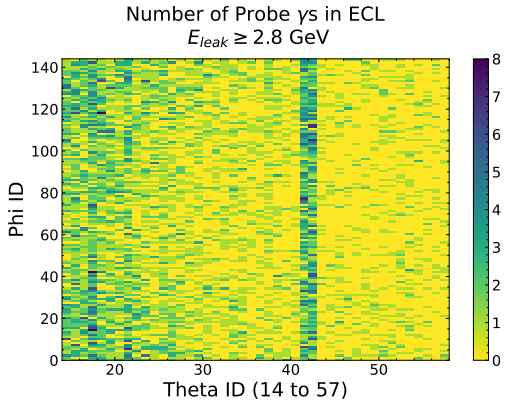

(e) $E_{\text{leak}} \geq 2.8\,\text{GeV}$

Figure 3.5: Number of photons per crystal in ECL for different leakage energies. Analysis conducted on MC13b Proc11 Exp10 $e^+e^- \to \gamma\gamma$ sample.

In order to assess the efficiency of the KLM, a matching procedure was done to see if any high leakage photons had gone through to the KLM and was reconstructed as a cluster. One can imagine a highly leaking photon punching through the ECL to reach the KLM. The KLM clusters per event were reconstructed as fake K_L particles in basf2, and an additional criterion listed below was used offline to ensure that these KLM clusters were from the high leakage photons.

- KLM cluster must have at least 2 layers
- Innermost layer of KLM is 1 or 2
- The position of the KLM cluster is within 25° of the lab frame 3D opening angle of the high leakage photon

Most of the neutron background particles only hit one KLM layer, so the two layers were required to avoid any other background particles. The innermost layer is the KLM layer closest to the ECL. The 25° cut was found by looking at the distribution of the 3D opening angle between an ECL cluster and a KLM cluster of the probe photon from an MC13b $e^+e^- \to \gamma\gamma$ sample. 25° was the optimal value.

In order to visually represent the efficiencies of the ECL and KLM, the percentage of the amount of leaking probe photons found in ECL that were also found in the KLM was plotted per crystal. Figure 3.6 shows the efficiencies depending on the leakage energy. For example, figure 3.6a shows that less than 10% of what was detected in the ECL was also detected in the KLM, whereas for higher leakages the efficiency significantly increases, where some of the crystals show 100%. However most of the yellow crystal bins in figure 3.6e indicate that there were no high leakage photons to begin with in the ECL. In addition, the figures also display the KLM geometry. The empty region at theta ID 54 with phi IDs between roughly 25 to 40 indicates the chimney region of the KLM, where there is no active detector material. There are also 8 horizontal lines, seen most clearly in figure 3.6a. This shows the octant structure of the KLM, where the 144 phi IDs in the barrel are split into 8 different regions with 18 phi ID crystals per section. The drop in efficiency shows that there are also no detector material in these gaps.

The overall conclusion from this study was that even if there is a highly leaking photon in the ECL, the KLM could identify the photon instead, hence the likelihood of both of the detectors missing a photon is low. There were also no significant inconsistencies between the sub-detector geometries.

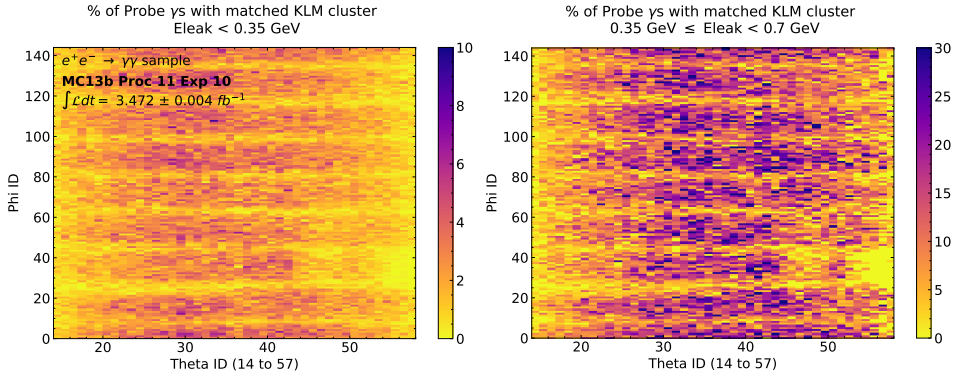

(a) $E_{\text{leak}} < 0.35\,\text{GeV}$ (b) $0.35\,\text{GeV} \leq E_{\text{leak}} < 0.7\,\text{GeV}$

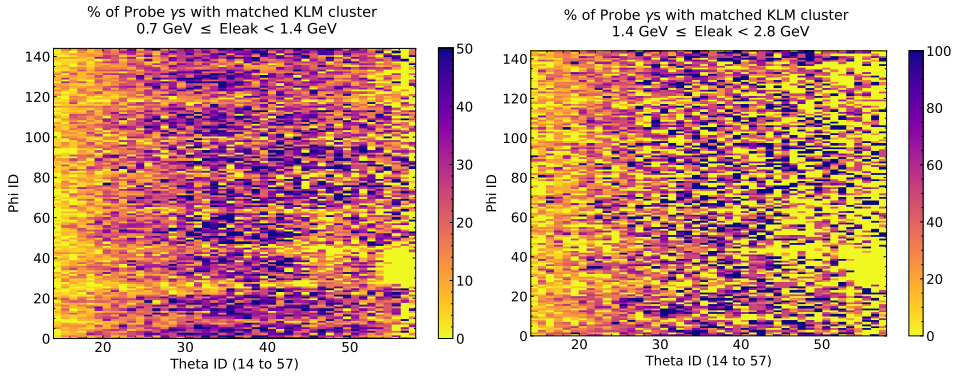

(c) $0.7\,\text{GeV} \leq E_{\text{leak}} < 1.4\,\text{GeV}$ (d) $1.4\,\text{GeV} \leq E_{\text{leak}} < 2.8\,\text{GeV}$

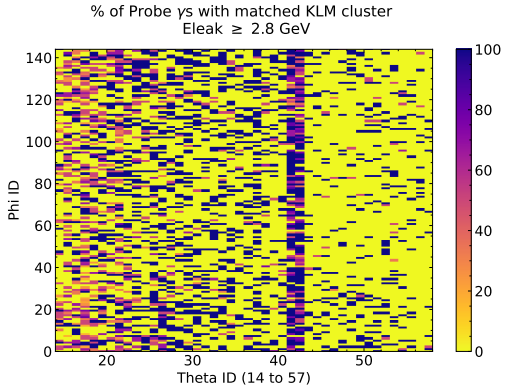

(e) $E_{\text{leak}} \geq 2.8\,\text{GeV}$

Figure 3.6: Percentage of photons per crystal in ECL which were matched with KLM clusters for different leakage energies. Analysis conducted on MC13b Proc11 Exp10 $e^+e^- \to \gamma\gamma$ sample.

3.3 Comparison between MC and data

In the previous section, efforts were made to look at the efficiencies of the ECL and KLM for MC events using the control sample $e^+e^- \to \gamma\gamma$. The same studies were then conducted on data corresponding to the MC13b events, which was expected to have the same efficiency. However, although the ECL efficiencies were similar, for every data-set studied, the KLM efficiency for data was always lower than what the MC13b projected. The left hand side of figure 3.7 shows the different KLM efficiencies for data and MC as a function of theta ID depending on the probe leakage energy. The right hand side then takes the ratio of data over MC for the KLM efficiency per theta ID. The average efficiencies for data and MC as well as the ratios are shown in table 3.3. For low leakage energy of $E_{\text{leak}} < 0.35\,\text{GeV}$, data only detects $26.52\% \pm 0.09\%$ of what MC13b does in the KLM, while for $E_{\text{leak}} \geq 2.8\,\text{GeV}$, this efficiency increases to $70.8\% \pm 0.6\%$. This is an improvement. Figure 3.8 represents the number of probe photons in ECL that were matched with a KLM cluster for $E_{\text{leak}} > 0\,\text{GeV}$. It is clear that some parts of the KLM were improved, as there was a firmware installation between data taking for experiment 8 and 10. Hence the KLM efficiency has improved overall, but has not yet reached its design efficiency. The numbers indicate how much the data needs to be scaled by MC if the detection of these leakage photons is lower in data. This studies is ongoing for experiment 12 data and MC.

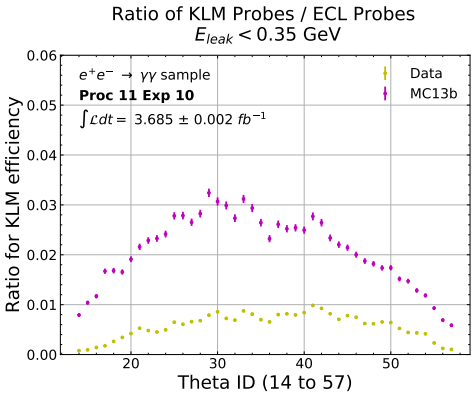

(a) $E_{\text{leak}} < 0.35\,\text{GeV}$

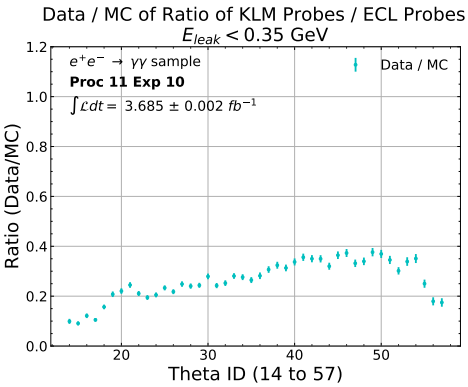

(b) Ratio of data over MC

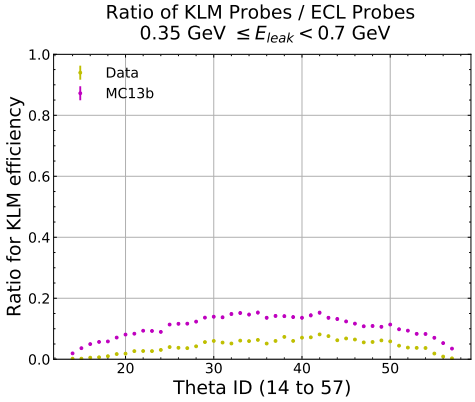

(c) $0.35\,\mathrm{GeV} \leq E_{\mathrm{leak}} < 0.7\,\mathrm{GeV}$

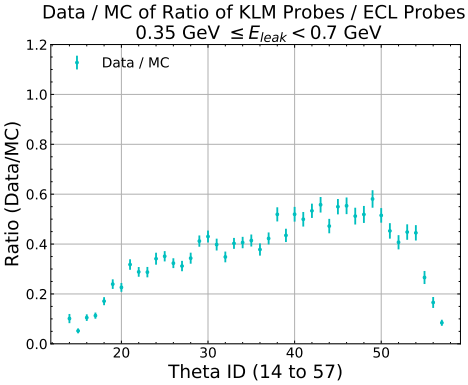

(d) Ratio of data over MC

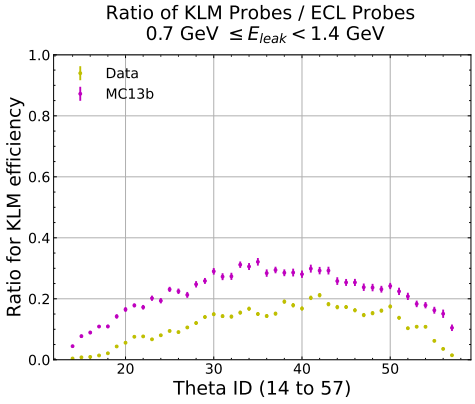

(e) $0.7\,\mathrm{GeV} \leq E_{\mathrm{leak}} < 1.4\,\mathrm{GeV}$

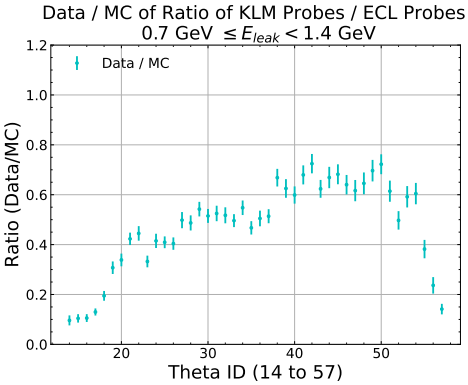

(f) Ratio of data over MC

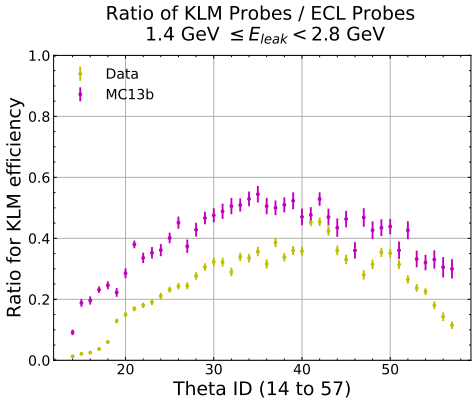

(g) $1.4\,\mathrm{GeV} \leq E_{\mathrm{leak}} < 2.8\,\mathrm{GeV}$

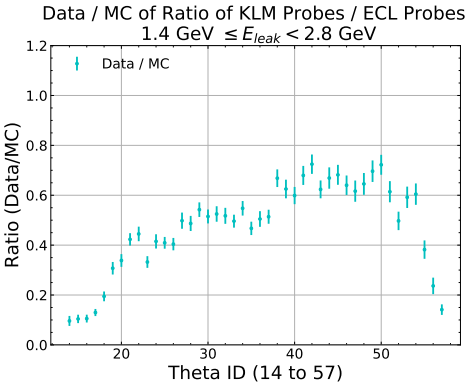

(h) Ratio of data over MC

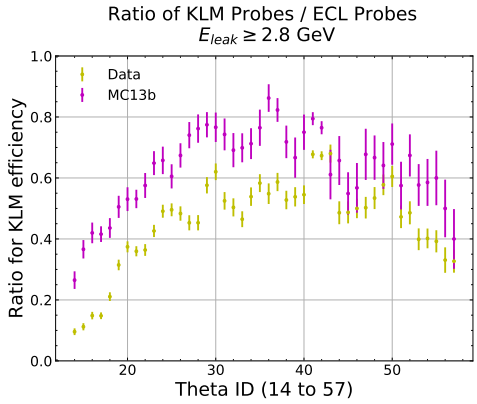

(i) $E_{\text{leak}} \geq 2.8\,\text{GeV}$

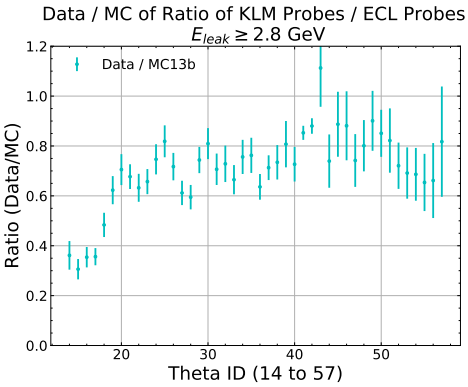

(j) Ratio of data over MC

Figure 3.7: The left hand side of the figures show the number of KLM clusters detected that were matched to a probe photon in ECL as a function of its theta ID for different leakage energies. The right hand side of the figures show the ratios of the KLM efficiencies for data over MC. Data and MC are scaled to have the same number of probes in the ECL.

Leakage Energy	Data Eff.	MC13b Eff.	Data/MC Ratio
$E_{\text{leak}} < 0.35\,\text{GeV}$	$0.573\% \pm 0.001\%$	$2.098\% \pm 0.004\%$	$26.52\% \pm 0.09\%$
$0.35\,\text{GeV} \leq E_{\text{leak}} < 0.7\,\text{GeV}$	$4.31\% \pm 0.01\%$	$10.61\% \pm 0.03\%$	$36.9\% \pm 0.2\%$
$0.7\,\text{GeV} \leq E_{\text{leak}} < 1.4\,\text{GeV}$	$11.495\% \pm 0.04\%$	$21.98\% \pm 0.07\%$	$47.7\% \pm 0.2\%$
$1.4\,\text{GeV} \leq E_{\text{leak}} < 2.8\,\text{GeV}$	$25.85\% \pm 0.08\%$	$39.7\% \pm 0.2\%$	$61.3\% \pm 0.3\%$
$E_{\text{leak}} \geq 2.8\,\text{GeV}$	$45.5\% \pm 0.2\%$	$62.9 \pm 0.4\%$	$70.8\% \pm 0.6\%$

Table 3.3: KLM efficiency for Proc11 Exp10 data and MC. Data and MC are scaled to have the same number of probes from the ECL.

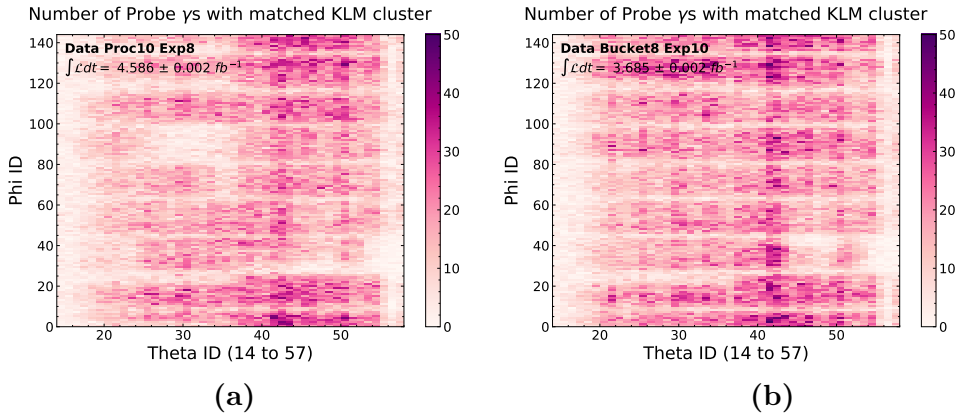

(a) **(b)**

Figure 3.8: **(a)** Number of probe photons in ECL matched with a KLM cluster for Proc10 Exp8 data. **(b)** Number of probe photons in ECL matched with a KLM cluster for Bucket8 Exp10 data.

In addition to the KLM efficiency, the energy distributions and leakage energies were also compared between data and MC. Figure 3.9 shows the CoM energy distribution for the probe photon of $e^+e^- \to \gamma\gamma$ sample taken from the ECL. There is clearly a difference between the number of probes found at low energies which are highly leaking for data and MC for both experiment 8 and 10. For Proc10 Exp8, data had 2.14 ± 0.04 times more entries of probes with $E^* < 2\,\text{GeV}$, while this number was 1.62 ± 0.03 for Proc11 Exp10. The low energy region is highly important as the signature becomes very similar to the dark photon events, with highly leaking photons mimicking as beam background photons. The overall efficiency however has improved between the experiments, as for energies near the peak of $E^* = 5.29\,\text{GeV}$, the ratio becomes nearly 1 between data and MC for experiment 10. This is possibly due to better calibration offline through processing the data. In order to investigate this issue further, Bhabha events were studied to see if there were any disagreements between data and MC.

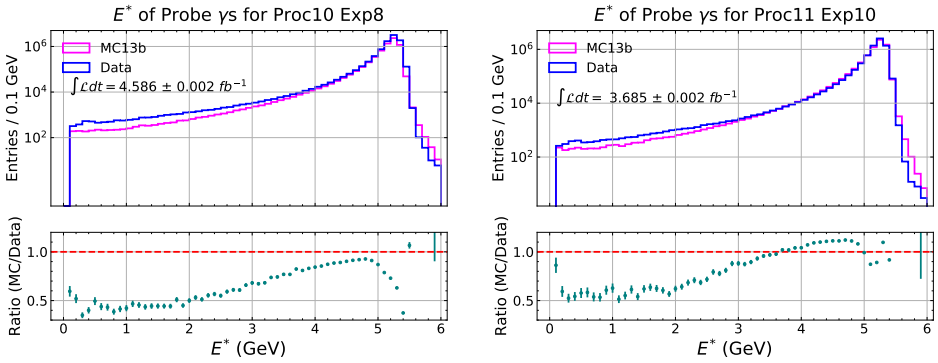

(a) **(b)**

Figure 3.9: **(a)** CoM energy of probe photons in Proc10 Exp8 data and MC. **(b)** CoM energy of probe photons in Proc11 Exp10 data and MC.

3.4 Bhabha events

In order to understand the difference between data and MC for high leakage probe photons, Bhabha events with signature $e^+e^- \to e^+e^-$ were also studied. The nature of the two types of background events are similar, as they produce two back-to-back particles, hence the comparison. Bhabha events have a high cross section of 300 ± 3 nb, when the electron or positron is within 10° to 170° in CoM polar angle, generated by BABYAGA.NLO [23]. The studies were conducted similar to the $e^+e^- \to \gamma\gamma$ events, where the electron and positron had to be back-to-back in both polar and azimuthal angle, and a tag and probe method was applied. The final cuts for selecting Bhabha events are listed below. p^* represents the momentum in the CoM frame.

First particle (take the particle with highest E^* in event):

- $E^* > 0.1\,\text{GeV}$
- $p_t > 0.2\,\text{GeV/c}$
- $p^* > 3.5\,\text{GeV/c}$
- $|d0| < 0.5\,\text{cm}$
- $|z0| < 4.0\,\text{cm}$
- Number of VXD hits > 0

- Number of CDC hits > 0

Second particle (choose the particle with the second highest E^* in event):

- $E^* > 4\,\text{GeV}$

For both particles:

- $\Delta\phi^* > 178°$
- $178° < \sum \theta^* < 182°$

By applying the cuts listed above, and further tagging an electron or positron with $E^* > 4.5\,\text{GeV}$, the difference between data and MC were found. As shown in figure 3.10, the difference in high leakage probe particles did not appear for Bhabha events as they did with $e^+e^- \to \gamma\gamma$ events. The middle peak for Bhabhas at $E^* = 3.5\,\text{GeV}$ is due to the cut of $p^* > 3.5\,\text{GeV}$.

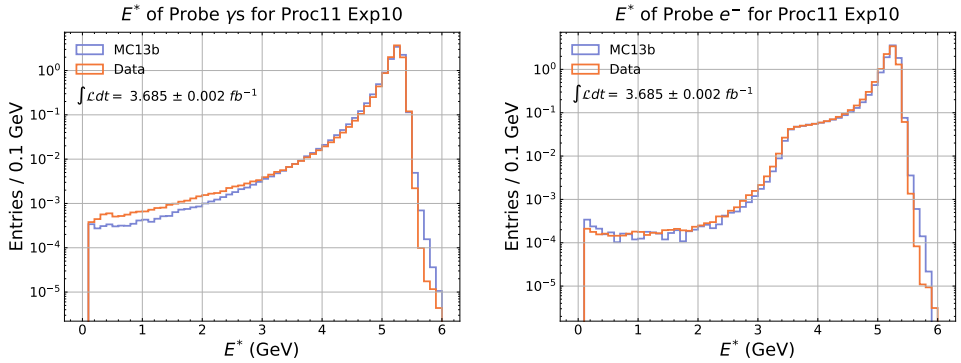

(a) **(b)**

Figure 3.10: **(a)** Number of probe photons in ECL as a function of CoM energy for Proc11 Exp10. **(b)** Number of probe electrons in ECL as a function of CoM energy for Proc11 Exp10.

Further studies were conducted on the angular distribution. Figure 3.11 shows how the highly leaking probes for Bhabha events mainly come from the 90° gap above the interaction point with theta ID 41 and 42. For Bhabha events, $38.6\% \pm 0.7\%$ of all high leakage probes were in either theta ID 41 or 42, while this number was $12\% \pm 2\%$ for $e^+e^- \to \gamma\gamma$ events. There is a lot more events in data than in MC for $e^+e^- \to \gamma\gamma$ events as these are high leakage photons.

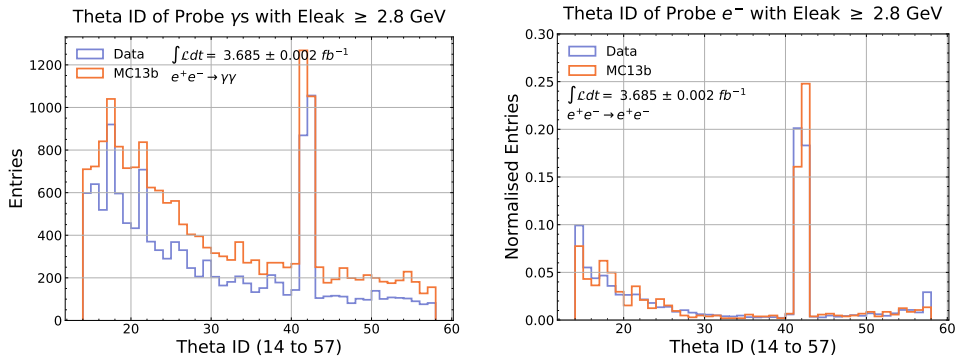

(a) $e^+e^- \to \gamma\gamma$. **(b)** $e^+e^- \to e^+e^-$.

Figure 3.11: **(a)** Number of probe photons in ECL as a function of theta ID for MC13b Proc11 Exp10. **(b)** Number of probe electrons in ECL as a function of theta ID for MC13b Proc11 Exp10.

The studies suggested that the data and MC disagreement is greatest for $e^+e^- \to \gamma\gamma$ events, where more highly leaking photons are present in data. Bhabha events are reconstructed through charged tracks, where the vertex detector and the CDC have better resolution than the ECL, which may provide an explanation for the better agreement in Bhabha events. However it was interesting to note the difference in distributions of highly leaking probes, where the 90° gap was the main source for Bhabha events. A different approach was necessary to understand the data and MC discrepancy.

3.5 Changing ECL geometry

Looking at the discrepancies between data and MC for high leakage photons, different distributions were performed based on position, seeing if there were any locations in the ECL that had less efficiency. Theta and phi both mainly showed a flat distribution, indicating no significance. A suggestion was made how the phi gaps could be bigger in the bottom half of the detector due to the gravitational force, however no immediate conclusions could be made. Furthermore, two new variables; local theta and local phi, were created for this studies. Local theta takes the position of the probe photons and projects the position of the cluster onto a single crystal. The distribution is shown in figure 3.12, where 0 indicates the lower theta edge of one crystal, while 1 indicates the higher theta edge of the same crystal. Most of the low energy particles only deposit its energy in one crystal, which the basf2 ECL

software will locate the cluster to be at the center of the single crystal. This is why there is a peak at the middle of the crystal, where the ratio between data and MC is much larger. In the region for local theta of 0.5 to 0.55, the ratio between MC and data was 0.53 ± 0.02. Similar to local theta, local phi maps the phi angle among 2 crystals next to each other in the azimuthal angle. This is because the 144 crystals in the same theta range are made of 2 crystals with the same structure that are replicated 72 times in the barrel. The 0 in local phi represents the lower phi range of the first crystal, while 2 represents the higher phi range of the second crystal. There is a large peak at 1, which indicates the gap between the two crystals, and this is also where the disagreement between data and MC is the highest. In the range of 0.975 and 1.025, the ratio between MC and data was 0.49 ± 0.02. The local phi disagreement strongly indicates that the gaps between individual crystals are bigger in the phi angle for data than in MC.

In order to test the theory of the ECL having larger gaps than in simulation, an attempt was made to move the crystals manually by simulation. The geometry module within basf2 was first manually updated by rewriting the positions of the crystals. The position of each crystal was written in Euler angles, which was rewritten in new numbers where the crystals were moved radially outwards by 5 mm and 10 mm. This increases the material gap in phi angles. In order to compare the differences in geometry, 10,000 $e^+e^- \to \gamma\gamma$ events were generated using a particle gun simulation in both the original geometry and the new shifted geometry.

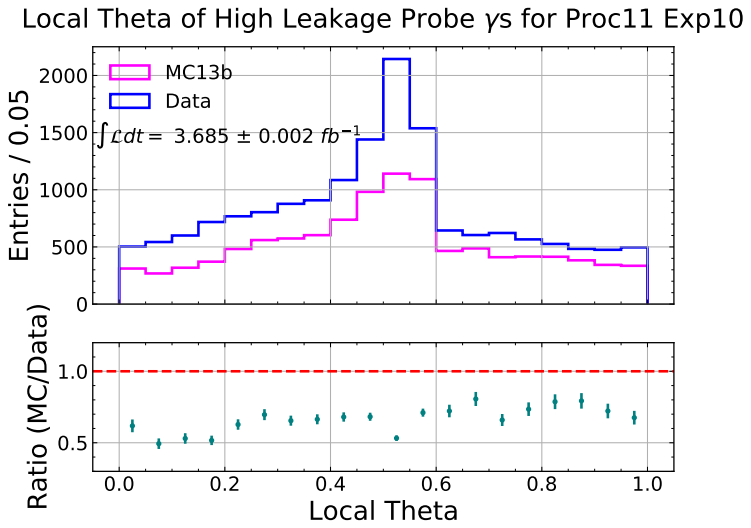

Figure 3.12: Local theta of high leakage probe photons for Proc11 Exp10 data and MC. The red line represents the ratio of MC to data as 1, representing perfect agreement.

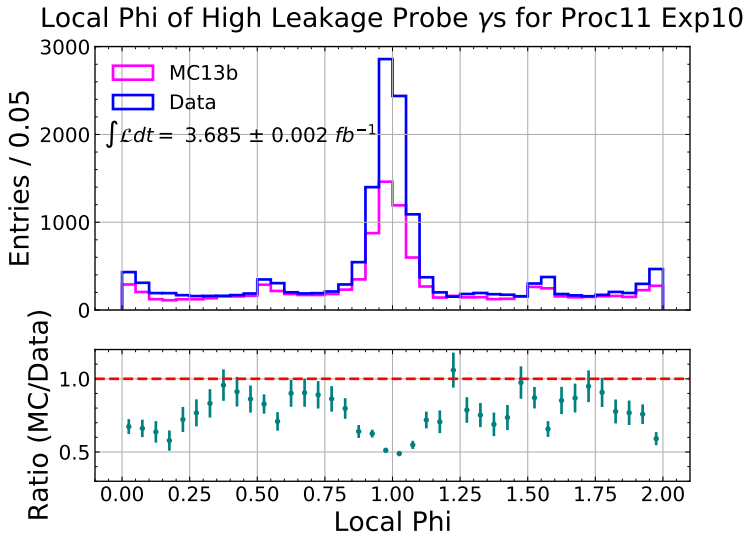

Figure 3.13: Local phi of high leakage probe photons for Proc11 Exp10 data and MC. The red line represents the ratio of MC to data as 1, representing perfect agreement.

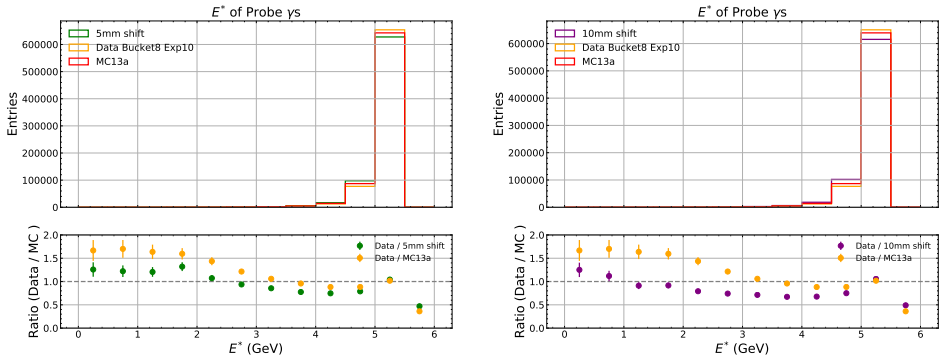

(a) **(b)**

Figure 3.14: **(a)** CoM energy of probe photon between MC13a, data Bucket8 Exp10, and 5 mm radially shifted crystals. The grey line represents the ratio of data to MC as 1, representing perfect agreement. **(b)** CoM energy of probe photon between MC13a, data Bucket8 Exp10, and 10 mm radially shifted crystals.

From figure 3.14, by comparing the CoM energy of the shifted and original geometry of the probe photons, it is clear that shifting the crystals does have an effect and improves the data and MC discrepancy. However, the overall distribution does not completely align as data, and the radial shift is not enough to conclude the problem. Three explanations for this phenomena were considered; background overlays, leakage correction, and skewed geometry. Background overlays are background events that are added to the MC samples, and are generated independently and added separately to the output. In order to recreate the same environment as data, the background overlays will also have to be generated using the different crystal geometry. However, after adding the background overlays, the changes were not significant and caused no difference. Hence this explanation was rejected. Leakage correction was also studied. When reconstructing photons, the energy distributions always show a low energy tail due to longitudinal and transverse leakage in the crystals, written more in detail in section 2.2.4. This can be modified with the appropriate use of clustering algorithms and taking the beam background into account. The corrections also help match the peak of the true photon energy between data and MC. Leakage corrections are always applied to the reconstructed quantities, and this effect was considered to affect the distribution of the probe photons. Instead of looking at the reconstructed cluster energy, the raw photon energies were studied instead. The raw photon energies are calculated by the weighted sum of all crystal

energies within an ECL cluster. The weight per crystal is less than 1 as there are cases of overlapping clusters and beam background events affecting the overall energy sum. The algorithm is made so that the width of the energy peak is minimised. An example of using the raw photon energy instead is shown in figure 3.15. UncorrE21 represents the uncorrected energy of the cluster energy scattered over 21 crystals. The 21 crystals represent the crystals in a 5×5 square of crystals where the 4 crystals at the edges of the square are not considered. The variable is divided by lab frame energy in order to account for the boost. Although both shifts showed better data and MC agreement, the trend did not follow that of the data and original MC13b geometry. Finally, there were suggestions of the crystals having a skewed geometry in data instead of a uniform radial shift outwards. Unfortunately the GEANT4 model limits the ability to move the crystals individually. Therefore this idea was not pursued. By moving the crystals, results did show that indeed crystals seemed to have bigger gaps in real life. However, moving the crystals outwards did not entirely solve the disagreement. The ratio between data and MC with shifted geometry did not perfectly align at 1. Rather than perfectly recreating the effect and rewriting the geometry positions, it was concluded that it would be better to find the scale factor between data and MC, and see how much scaling is necessary to predict background events from MC events to match the expectation in data.

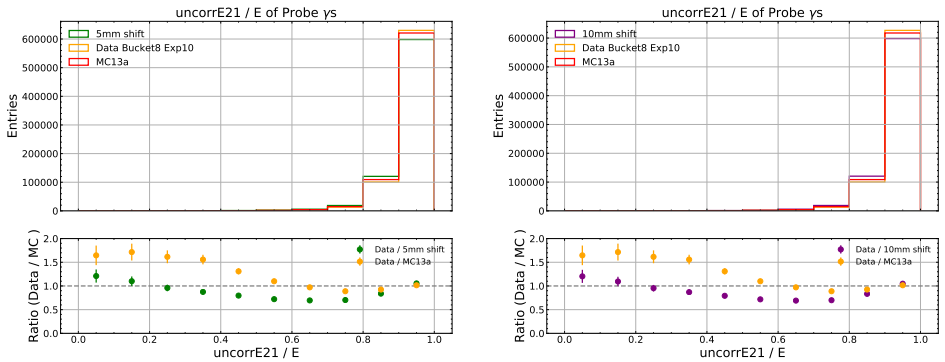

(a) **(b)**

Figure 3.15: **(a)** UncorrectedE21/E of probe photon between MC13a, data Bucket8 Exp10, and 5 mm radially shifted crystals. The grey line represents the ratio of data to MC as 1, representing perfect agreement. **(b)** UncorrectedE21/E of probe photon between MC13a, data Bucket8 Exp10, and 10 mm radially shifted crystals.

3.6 Signal analysis

Further studies were conducted by using dark photon signal events. By introducing signal events, a newly defined set of cuts were introduced for high leakage probe photons based on the skim cuts applied for the single photon selection. A skim in Belle II is a script which further reduces the number of events after the trigger. Currently the skim for dark photon includes a cut where the second cluster in an event aside from the single photon can only have $E < 0.55\,\text{GeV}$. In the previous sections, the probe photon in the $e^+e^- \to \gamma\gamma$ control sample had a leakage energy of $E_{\text{leak}} \geq 2.8\,\text{GeV}$. This new cut is an even tighter cut on the high leakage for probe photons as they only deposit $E^* < 0.55\,\text{GeV}$ out of the $4\,\text{GeV}$ to $7\,\text{GeV}$ that they usually have from the $e^+e^- \to \gamma\gamma$ event. A similar efficiency study conducted in section 3.3 was also conducted for the new high leakage probe photons. If the probe particle was not detected, then the tag particle will be the only particle in the event, which could either be the signal dark photon event or when one of the photons from $e^+e^- \to \gamma\gamma$ was missed. In order to avoid un-blinding and seeing any signal in data, the energies of the probe photon was taken at $0.1\,\text{GeV} < E^* < 0.55\,\text{GeV}$, ensuring that there are two photons per event. The ratio between the new high leakage probes to all probe photons as a function of tag theta ID is illustrated in figure 3.16a. Previously the ratios were taken as a function of probe theta ID. For signal events, the single photon acts as a tag photon while the invisible dark photon acts as a probe photon in comparison to $e^+e^- \to \gamma\gamma$ events. Hence tag photons were considered to avoid un-blinding. As previous sections state, there are more higher leakage photons in data than in MC which is represented in figure 3.16b, where on average there were 3.1 ± 0.3 times more entries in data than in MC for regions excluding theta ID 28 and 29. The theta ID 28 and 29 represent when the probe photon is in theta ID 41 and 42, which are where the 90° ECL gap is. For when the theta ID was 28 or 29 for the tag photon, the agreement between data and MC was much better, with 0.999 ± 0.003. The final ratios which is necessary to scale the MC prediction for background events are currently being conducted on Buckets 9-15 Exp12 data and MC. The KLM efficiency was also studied by checking the amount of KLM clusters that matched to the probes found in the ECL, with the same criteria listed in section 3.2. The ratio as a function of tag theta ID can be seen in figure 3.17a, while the data and MC ratio is displayed in figure 3.17b. The small statistics has made the uncertainties much higher. The higher leakage shows the increase in efficiency, and there were 0.80 ± 0.08 times as much entries for data than in MC without theta ID 28 and 29. The

efficiency was 0.913 ± 0.002 for theta ID 28 and 29. This shows how the efficiency for the KLM is still less than expected, but overall has improved compared to less leaked photons. The regions of theta ID 28 and 29 agree well for both the ECL and KLM, indicating that the ECL has good alignment agreement. This may however change, as a small adjustment was recently made by moving the beampipe alignment for the new software release [52], which may affect this analysis in the future.

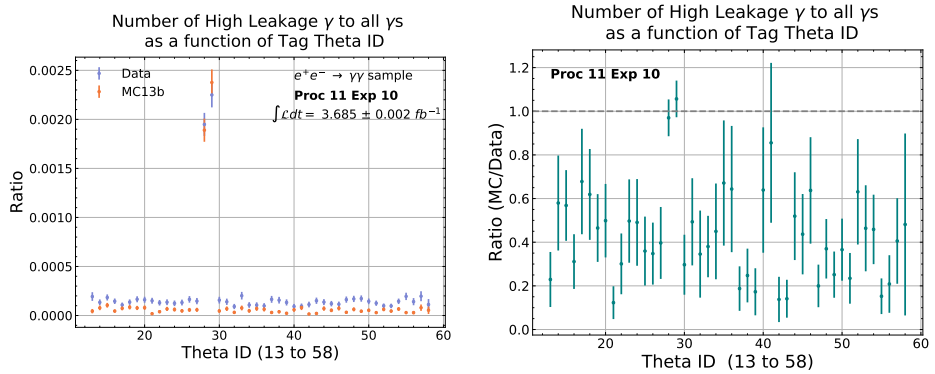

(a) (b)

Figure 3.16: **(a)** Ratio of number of high leakage probe photons to all probe photons as a function of tag theta ID. **(b)** Ratios between Proc11 Exp10 data and MC for ratios of high leakage probe photons to all probe photons. The grey line indicates that the ratio of MC to data is 1, which signifies good agreement.

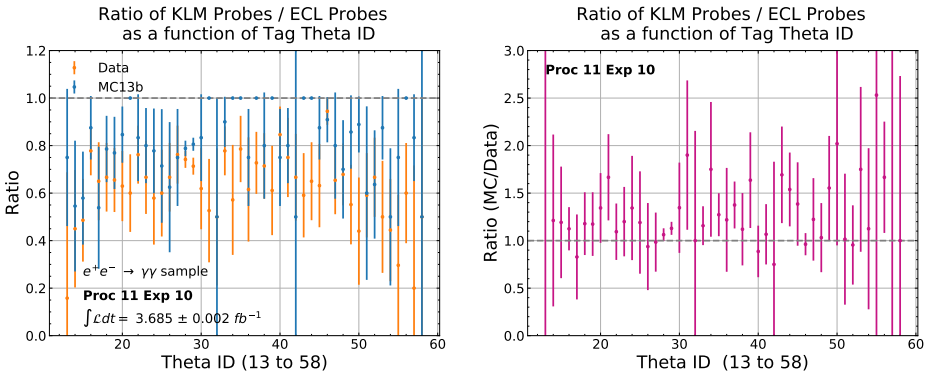

(a) (b)

Figure 3.17: **(a)** Ratio of KLM probe photons to ECL probe photons as a function of tag theta ID. **(b)** Ratios between Proc11 Exp10 data and MC for ratio of KLM probe photons to ECL probe photons as a function of tag theta ID. The grey line indicates that the ratio of MC to data is 1, which signifies good agreement.

In order to account for the signal selection, new cuts were introduced which were applied on both signal MC with $m_{A'} = 0.05\,\mathrm{GeV/c^2}$ and $e^+e^- \to \gamma\gamma$ events using data and MC listed below. The ntuple was remade. As both signal and background events are being used, the signal photon and tag photon in events were all relabelled as candidate photon. $|dz|$ represents the distance between the point of closest approach to the z axis and the IP.

Event cut:

- No charged particles with $|dz| < 10\,\mathrm{cm}$ and $p_t > 0.15\,\mathrm{GeV/c}$ per event
- There can be no other particle with $E > 0.55\,\mathrm{GeV}$ other than the candidate photon per event

Candidate photon:

- Must be in barrel region
- $E^* > 4.9\,\mathrm{GeV}$
- There can only be one particle which satisfies the candidate photon cut per event

Second most energetic photon in event:

- The second most energetic photon in an event must satisfy the event cut listed above.

Most back-to-back photon with candidate photon in event:

- The most back-to-back photon with the candidate photon per event must have $E > 0\,\text{GeV}$.

Most back-to-back KLM cluster with candidate photon in event:

- The most back-to-back KLM cluster with the candidate photon per event must have at least 1 layer.

The most significant change made with respect to the control sample cuts was splitting the probe photon into the second most energetic photon in event and the most back-to-back photon to the candidate photon in event. Previously for the $e^+e^- \to \gamma\gamma$ control sample, the second most energetic photon was automatically identified as the most back-to-back photon, as this is mostly the case. However if the most back-to-back photon is highly leaking, the second most energetic photon may be a beam background photon instead, hence it was important to separately identify these photons. Most of the time however, the second most energetic and most back-to-back are the same photon. In addition, a small change was made on the charged track cuts. Previously it was $|d0| < 2\,\text{cm}$, but in order to keep conversion events where one or both the photons convert into an e^+e^- pair, only the tracks coming from the IP are vetoed.

With the cuts above, for MC13b Proc11 Exp10 events, $23.3\% \pm 0.1\%$ of entries looked exactly like single photon events, where the most back-to-back and second most energetic photon had empty entries, which led to making further cuts to reduce background events. The theta range for the candidate photon was reduced further down from theta ID between 16 to 27, and 30 to 53. This is to ensure that the most back-to-back photon is within barrel and away from the endcap gaps, and also to avoid theta ID 28 and 29 for the candidate photon as this is where the most back-to-back photon goes into the 90° gap. Figure 3.18 shows a 2D histogram of the position in theta ID of the candidate photon and the most back-to-back photon. The regions enclosed by the orange lines are the newly defined region for the candidate photon.

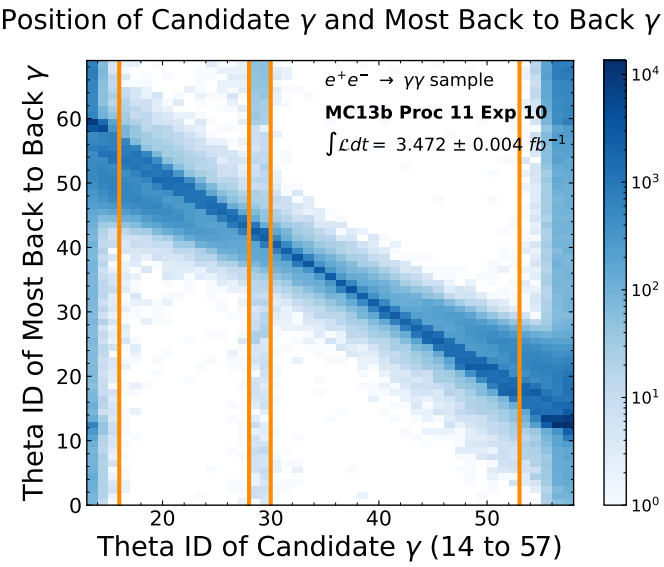

Figure 3.18: Theta ID of candidate photon against most back-to-back photon for MC13b Proc11 Exp10 using $e^+e^- \to \gamma\gamma$ control sample. The region enclosed by the orange lines are theta ID between 16 to 27, and 30 to 53, which is the defined region for the candidate photon.

Signal events were added to further modify the selection criteria. 20,000 events were generated using MadGraph5 [45] with mass of $m_{A'} = 0.05\,\mathrm{GeV/c^2}$ for the dark photon. In order to quantify the best cut between signal and background, the Punzi variable [53] was used as the figure of merit. The Punzi variable uses equation 3.3 in order to quantify the optimal cut value between background and signal events, where ϵ_s is the efficiency of the signal events and B is the expected background events scaled by luminosity. a represents the number of sigmas corresponding to a one sided Gaussian test at a given significance, which has been set to $a = 5$. An example of the Punzi distribution can be seen for figure 3.19 for finding the optimal cut for the energy of the second most energetic photon.

$$\text{Punzi Figure of Merit} = \frac{\epsilon_s}{\frac{a}{2} + \sqrt{B}} \tag{3.3}$$

By optimising the cuts with Punzi, the final selections were chosen:

- Most back-to-back photon to candidate photon has either $E \leq 0.03\,\mathrm{GeV}$, or has opening angle $< 160^\circ$
- Second most energetic photon has $E < 0.25\,\mathrm{GeV}$
- The number of most back-to-back KLM cluster with candidate photon can be either 0, or if there were a cluster, it must have an opening angle $< 46^\circ$

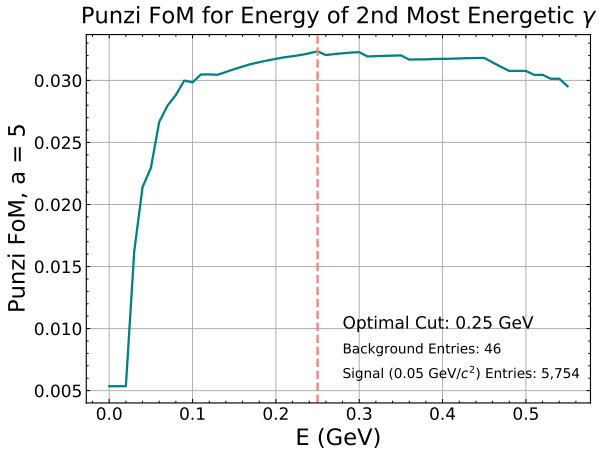

Figure 3.19: Punzi figure of merit for energy of second most energetic photon using MC13b Proc11 Exp10 and signal events with $m_{A'} = 0.05\,\mathrm{GeV/c^2}$. The red line signifies the Punzi optimal value which was 0.25 GeV.

After adjusting the events with the cuts using MC13b Proc11 Exp10, there were only 2 events remaining out of the 83,910 events, which showed promising results of being able to remove the background events entirely, including those which look similar to signal events. However these cuts were applied to MC13b Buckets 9-15 Exp12, which unfortunately showed that events could not be eliminated with higher luminosity and more beam background events. There were 2,578 events remaining out of 1,576,905 events, which is 88 times more than the prediction from experiment 10 when scaling with luminosity. The differences between the MC13b samples are shown in figure 3.20, which is before any of the additional cuts from Punzi listed above are applied. The different distributions suggested that there were excess events in theta ID 16 to 27 for the candidate photon in experiment 12. Further analysis showed that these were beam background events which are the same photons that are causing the large peak at 1 for the number of KLM layers. The distributions look identical when the photons are matched to what was generated in the MC file, which shows how the selection criteria is not enough to reduce the beam background events. The events generated seemed to not have any problems, but somehow the selection criteria chose the beam background photons instead of the ones generated. The cause is still being investigated. This study is ongoing with an $e^+e^- \to \gamma\gamma$ sample of 100 fb^{-1} with MC14a production, which showed an agreement to MC13b Proc11 Exp10. Furthermore, in order to investigate this effect, the corresponding data was also studied, presented in section 3.7.

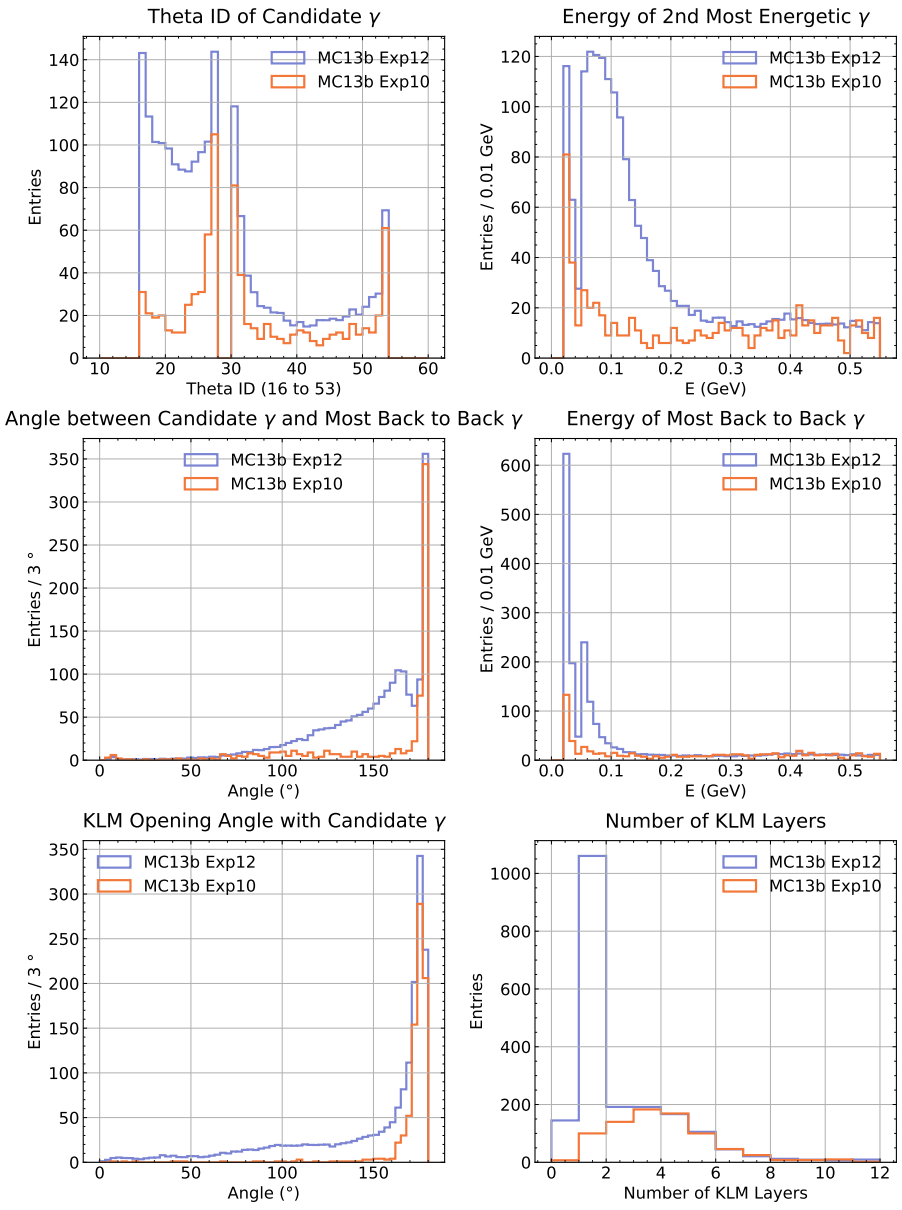

Figure 3.20: MC13b Proc11 Exp10 and MC13b Buckets 9-15 Exp12 comparison with relevant variables using the control sample of $e^+e^- \to \gamma\gamma$ events. The entries have been scaled by luminosity.

3.7 Cosmics and pin diode studies

In order to understand the discrepancies found between MC13b experiments 10 and 12 in section 3.6, the corresponding data was studied. However, when looking at the entries stored in the ntuple before any additional cuts were applied, there were many entries above $E > 7\,\text{GeV}$ for the candidate photon, which are kinematically impossible. The distribution is displayed in figure 3.21, where there is a large peak at 20 GeV. This signature for data was present in both experiments 10 and 12. Therefore before any of the analysis conducted in section 3.6 was performed, it was important to eliminate these events with excess energy first and have a clear sample of $e^+e^- \to \gamma\gamma$ events.

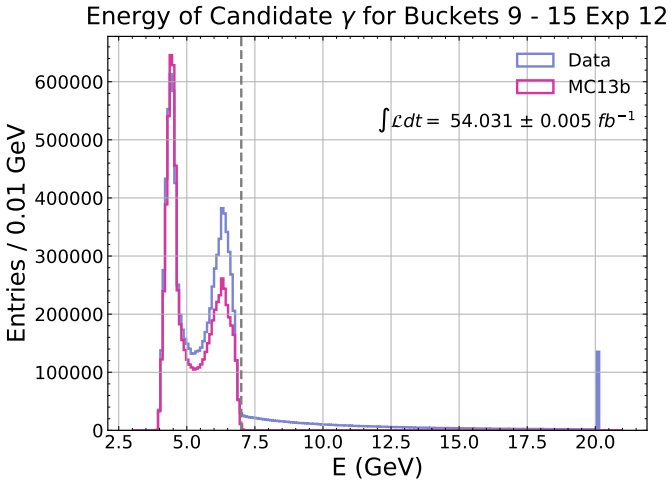

Figure 3.21: Energy of candidate photon for Bucket 9-15 Exp12 data and MC. The grey line is at 7 GeV, where entries above this value could not have come from the e^+e^- collisions.

The source of these entries were considered to be cosmic rays and pin diode events, where their energies could be anything as they are not restricted by the beam energy. There is a sharp peak at around $E = 20\,\text{GeV}$ as any energy above 20 GeV gets stored at a particular value of 20.085 GeV.

Cosmic rays are mainly high energy protons and other atomic nuclei coming from outer space. They range between different energies, and flux increases with lower energies. Pin diode events are caused by beam particles hitting the material of the sub-detectors. The neutrons and protons of the material get excited and produce a delta resonance, which further produces a low energy neutron. This neutron then only hits the pin diodes of the

calorimeter and nothing else. The pin diodes are normally used to convert the light in the crystal as energy, where the pin diodes register a very small amount of energy per cluster. However, when a neutron hits a pin diode directly, the pin diode registers a large amount of energy, which then is accidentally identified as a high energy cluster.

In order to try and eliminate both signatures, appropriate variables were used for additional cuts. The cuts were optimised using data, MC, signal, single beam events, and cosmic ray events. The cosmic ray events were taken during experiment 16 and experiment 18 where no beams were running, and was taken for a total duration of 3 days, 12 hours, 45 minutes, and 44 seconds. For single beam events, data was collected only when the LER or HER was running, however the statistics were small and effects concerning cosmic and pin diode events were negligible and was not included in the final analysis presented here. In order to avoid un-blinding, events with either $E^* > 5.5\,\text{GeV}$ or $E > 20\,\text{GeV}$ was analysed, as these events could not be single photon events nor $e^+e^- \to \gamma\gamma$.

For cosmic rays, the ZernikeMVA variable, KLM cluster closest to candidate photon, and particles with transverse momentum were analysed.

ZernikeMVA uses the distribution of shower shapes by looking at Zernike moments to discriminate different particles. Minimum ionizing particles like muons only deposit their energy in one or two crystals, whereas photons create symmetric showers with most of its energy deposit in the middle [54]. The significance of this variable can be found in figure 3.22, where the distributions are vastly different between cosmic events and MC events, where a high ZernikeMVA value represents a good photon coming from the IP.

Furthermore, there is a high likelihood of through going cosmic rays which goes through one side of the detector and continues to go out through the opposite side. In this case, two KLM clusters could be found in an event, hence in addition to the most back-to-back KLM cluster with the candidate photon, the KLM cluster closest to the candidate photon was also stored. Rather than a photon coming from the ECL and leaking through to the KLM, the cosmic ray would enter the KLM and leak through to the ECL. Between the two clusters, the "best KLM cluster" was stored by choosing the cluster with most layers. Figure 3.24 presents the 2D histogram of the best KLM layer against the opening angle with the candidate photon of the best KLM layer. For data and cosmic events, it is clear that the candidate photon has a KLM cluster close by which goes through many layers, while for MC events there was leakage from the most back-to-back photon. Signal also has some minor leakage from the single photon although this effect was

small. In the end, only the number of KLM layers of the best KLM cluster was used for the cut, regardless of the position of the cluster with respect to the candidate photon.

The particle with the highest transverse momentum per event was also considered, as there may be cases when the cosmic ray goes through the CDC and vertex detectors. However most events did not have an entry, which may be that the cosmic rays are coming at such an angle which the tracking sub-detectors cannot observe. For data with candidate photons $E^* > 5.5\,\text{GeV}$, $82.71\% \pm 0.03\%$ of ntuple entries had no entries for this particle, while this number was $80.5\% \pm 0.1\%$ for cosmic events. Therefore this is a very loose cut.

For pin diode events, the time of cluster was considered. Normally when there is scintillation in the calorimeter, there is a decay time of roughly 1 µs, however the pin diode events would have a delta function at a specific time since there is no EM shower. The time for a particle is calculated through multiple steps using sub-detectors. Firstly, the time of the particle with the largest energy deposit will be recorded and a value will be subtracted to be adjusted at $t = 0\,\text{ns}$. Secondly, the time for the other particles in the event will also be subtracted by the same amount. Therefore if there were particles out of time with the most energetic particle, it would not peak at 0 ns. Figure 3.23 shows the timing distribution of the candidate photons. There is a small bump at around $-250\,\text{ns}$, which suggests pin diode events, and the appropriate value was found as a cut.

The final selection for removing cosmic and pin diode events became:

- Charged particle with highest p_t per event must have $p_t < 1\,\text{GeV/c}$
- Time of candidate photon must be $-150\,\text{ns} < \text{time} < 150\,\text{ns}$
- Candidate photon has ZernikeMVA ≥ 0.5
- The number of layers for the best KLM cluster is ≤ 5

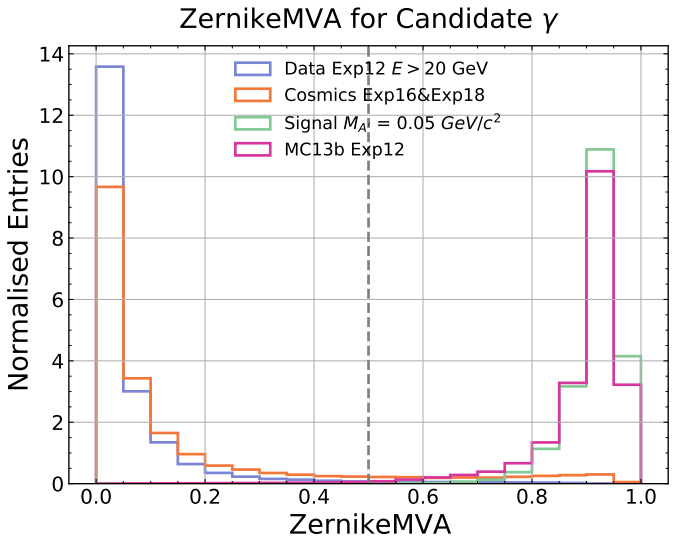

Figure 3.22: ZernikeMVA distribution of candidate photon for signal, cosmic, data, and MC $e^+e^- \to \gamma\gamma$ events. The grey line is at 0.5, where anything above this value is stored as a candidate event.

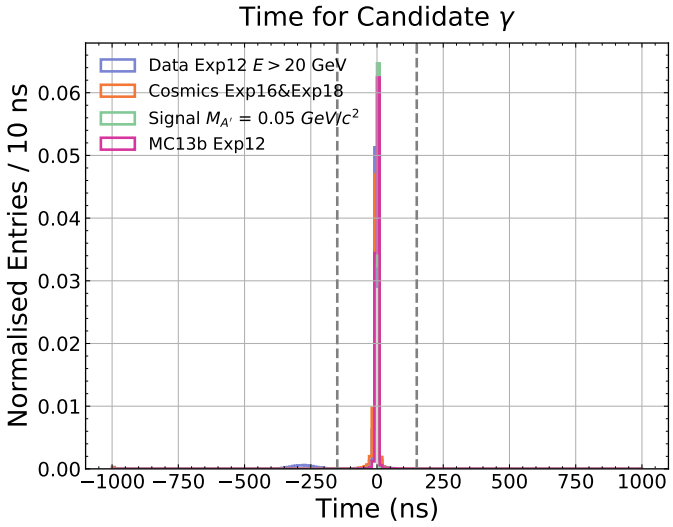

Figure 3.23: Time distribution of candidate photon for signal, cosmic, data, and MC $e^+e^- \to \gamma\gamma$ events. The grey lines are at -150 ns and 150 ns, where any candidate photon that falls within this time will be stored as a candidate event. There is a small peak at around -250 ns from the pin diode events.

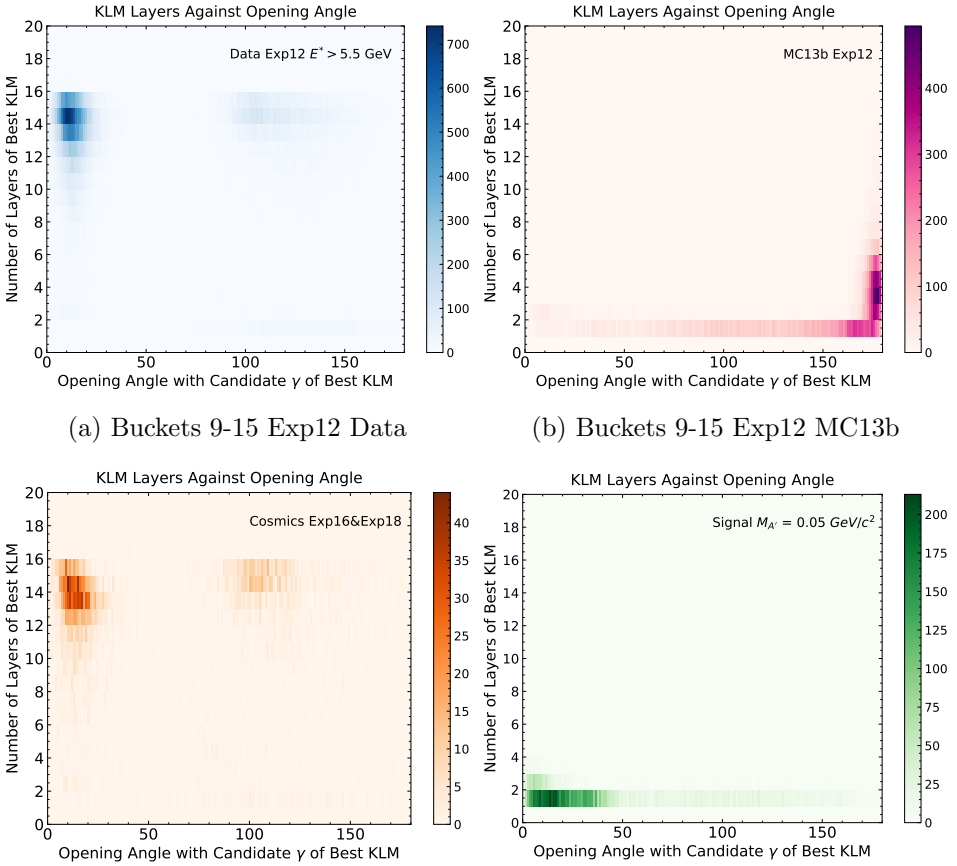

(a) Buckets 9-15 Exp12 Data

(b) Buckets 9-15 Exp12 MC13b

(c) Exp16 and Exp18 cosmic events

(d) Signal events with $m_{A'} = 0.05\,\mathrm{GeV/c^2}$

Figure 3.24: Number of KLM layers against opening angle of best KLM cluster with candidate photon for signal, cosmic, data, and MC $e^+e^- \to \gamma\gamma$ events.

Cut	KS test statistic	p value
Pass ZernikeMVA Fail KLM	0.016	5.4×10^{-2}
Pass KLM Fail ZernikeMVA	0.026	2.4×10^{-4}
Pass ZernikeMVA Pass KLM	0.18	7.1×10^{-5}
Fail ZernikeMVA Fail KLM	0.0073	2.0×10^{-3}

Table 3.4: Results of Kolmogorov–Smirnov test for Exp16 and Ep18 cosmic events and Buckets 9-15 Exp12 data.

The goal for applying these cuts were to take out the cosmic and pin diode events from the background sample, enabling a clear sample of $e^+e^- \to \gamma\gamma$ events. However, even with these additional cuts, this was not enough to suppress the cosmic events. 3,902 events out of 1,387,276 events were left remaining after the additional cuts listed above for data with $E^* > 5.5\,\text{GeV}$, while this number was 215 events out of 118,793 events for the Exp16 and Exp18 cosmic events. Hence the final step was to find the number of cosmic events expected to be in the energy range of $4.9\,\text{GeV} \leq E^* < 5.5\,\text{GeV}$ where the events interfere with the $e^+e^- \to \gamma\gamma$ background and signal events. In order to make a prediction, the last two selection criteria using ZernikeMVA and best KLM layer were used, after the other cuts have already been applied. There are four ways which an event can be categorised using these two cuts; events which pass ZernikeMVA cut but fail the best KLM layer cut, events which pass the best KLM layer cut but fail the ZernikeMVA cut, events which pass both ZernikeMVA and best KLM layer cuts, and events which fail both the ZernikeMVA and best KLM layer cuts. Passing would mean a higher likelihood of the events being either a signal dark photon event or a $e^+e^- \to \gamma\gamma$ event, while failing will mean a higher likelihood of being a cosmic or a pin diode event. These cuts were applied for both cosmics and data per energy bin, starting from 4.9 GeV and ending at 24.5 GeV. The full breakdown of the numbers is shown in A.1 and A.2. The idea of this table was to use the numbers above 5.5 GeV to predict entries below 5.5 GeV for data by comparing it with cosmic events.

This prediction heavily relies on the fact that the distributions per cut would be the same for both data and cosmic events. In order to ensure this, a double sided Kolmogorov–Smirnov (KS) test using the scipy package was performed [55]. The results of the KS test is shown in table 3.4. The KS test unfortunately did not show a strong correlation between the two data-sets, however the analysis was continued. A visual representation of the similarity between the two data-sets is shown in figure 3.25, where other than the pass

ZernikeMVA and pass KLM cut, they all look similar. The problem with the pass ZernikeMVA and fail KLM cut is that there is a large interference with the $e^+e^- \to \gamma\gamma$ events. For MC events, in the $4.9\,\text{GeV} < E^* \leq 5.5\,\text{GeV}$ range, there were 16,825 entries out of the total 2,774,756 for all four cuts. In order to account for this, the amount of entries from the MC prediction was subtracted from the data entries as they have the same luminosity, in order to obtain a clean cosmic sample. The numbers seen in A.1 and A.2 are the final numbers after subtraction. It is also important to note that there were roughly $5.547\% \pm 0.001\%$ events for MC with energies $5.5\,\text{GeV} < E^* \leq 6.5\,\text{GeV}$ which may result from resolution and calibration, which was also subtracted from data.

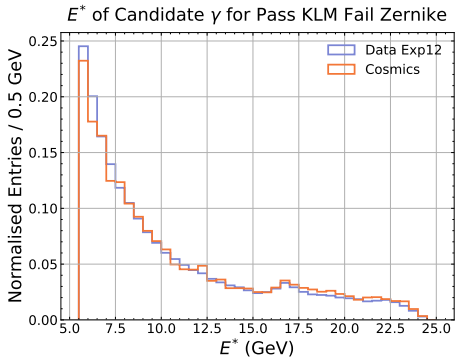

(a) Pass KLM cut and fail ZernikeMVA cut.

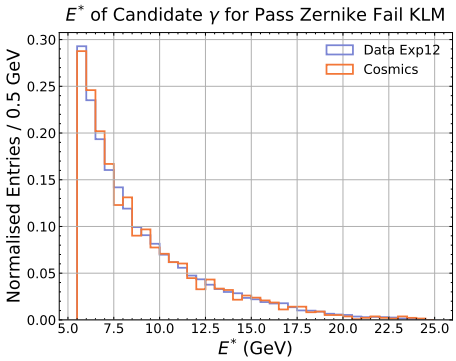

(b) Pass ZernikeMVA cut and fail KLM cut.

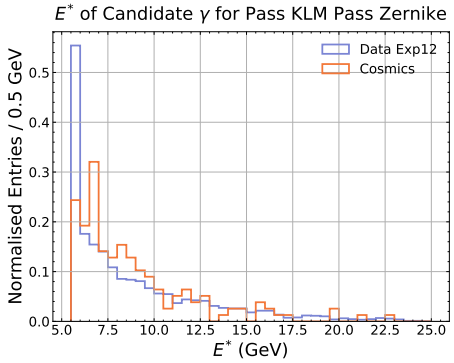

(c) Pass ZernikeMVA cut and pass KLM cut.

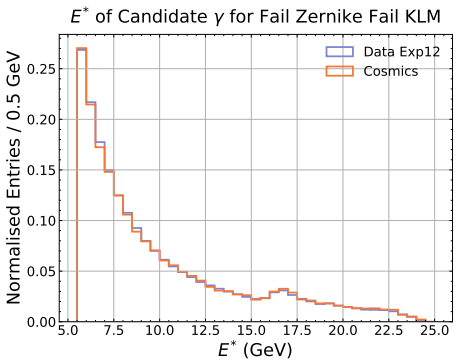

(d) Fail ZernikeMVA cut and fail KLM cut.

Figure 3.25: CoM energy of candidate photon for cosmic and data events with different cuts.

There were three different methods considered to make the prediction. All methods rely on a scale factor (SF) and a base number (BN). The scale factor tries to scale the amount of events expected from cosmic events to data. The base number is the number that the scale factor is multiplied by to make the final prediction. All methods follow the simple model of base number $\times$ scale factor = expected number of events. The detailed version of the methods are listed below, where $\sum$ signifies the sum of all events with the particular criteria. Method 1 uses and compares data and cosmics, method 2 only uses data to lower the uncertainties as data has much more statistics, and method 3 compares data and cosmics but only using one energy bin. The "with cuts" signifies the four different cuts, where method 1 iterates all four different cuts, while method 2 and 3 uses everything except when it passes both cuts.

- Method 1:
  - **BN:** $\sum 4.9\,\text{GeV} < E^* \leq 5.5\,\text{GeV}$ that pass both cuts for cosmics
  - **SF:**

$$\frac{\sum E^* > 5.5\,\text{GeV with cuts for data}}{\sum E^* > 5.5\,\text{GeV with cuts for cosmics}} \tag{3.4}$$

- Method 2:
  - **BN:** $\sum 4.9\,\text{GeV} < E^* \leq 5.5\,\text{GeV}$ with cuts for data
  - **SF:**

$$\frac{\sum E^* > 5.5\,\text{GeV with cuts for data}}{\sum E^* > 5.5\,\text{GeV that pass both cuts for data.}} \tag{3.5}$$

- Method 3:
  - **BN:** $\sum 4.9\,\text{GeV} < E^* \leq 5.5\,\text{GeV}$ that pass both cuts for cosmics
  - **SF:**

$$\frac{\sum 4.9\,\text{GeV} < E^* \leq 5.5\,\text{GeV with cuts for data}}{\sum 4.9\,\text{GeV} < E^* \leq 5.5\,\text{GeV with cuts for cosmics}} \tag{3.6}$$

The results of each method using different cuts are listed in table 3.5. The validation ratio is measure of ratio of the final predicted number to all the events with $E^* \geq 5.5\,\text{GeV}$ in data, which was a fixed number of $3,537$

events in data. The same ratio for cosmics events was 0.205 ± 0.002, which was used as a way to validate the final result.

	Method 1	**Validation Ratio**
Pass ZernikeMVA Fail KLM	599 ± 107	0.169 ± 0.007
Pass KLM Fail ZernikeMVA	624 ± 111	0.176 ± 0.007
Pass ZernikeMVA Pass KLM	726 ± 141	0.205 ± 0.008
Fail ZernikeMVA Fail KLM	454 ± 80	0.128 ± 0.006
	Method 2	**Validation Ratio**
Pass ZernikeMVA Fail KLM	1240 ± 24	0.35 ± 0.01
Pass KLM Fail ZernikeMVA	665 ± 12	0.188 ± 0.007
Fail ZernikeMVA Fail KLM	733 ± 12	0.207 ± 0.008
	Method 3	**Validation Ratio**
Pass ZernikeMVA Fail KLM	948 ± 172	0.268 ± 0.009
Pass KLM Fail ZernikeMVA	677 ± 121	0.191 ± 0.007
Fail ZernikeMVA Fail KLM	468 ± 83	0.132 ± 0.006

Table 3.5: Results and validation ratio of prediction for all methods and cuts in Buckets 9-15 Exp12 data.

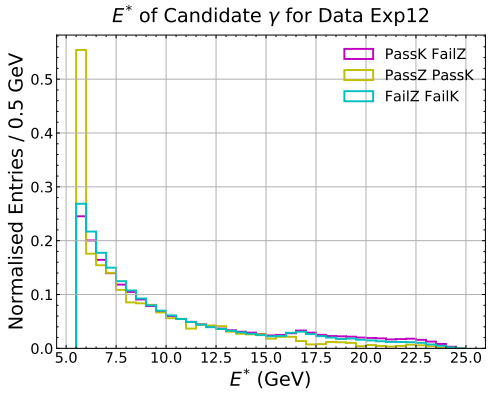

Figure 3.26: CoM energy of candidate photon for Buckets 9-15 Exp12 data for different cuts. The pass ZernikeMVA and pass KLM cut has a distribution different from the other two cuts.

Although all of the different methods were explored, some of the estimates were deemed unsuitable. The distributions for the pass ZernikeMVA and fail KLM events showed that there was a lot of mixture of the $e^+e^- \to \gamma\gamma$ that could not be removed, and was therefore completely eliminated from the final estimate. Method 2 relies on the distributions of the pass ZernikeMVA and pass KLM cut in data being the same as other cuts, however this was not the case, shown in figure 3.26. This may also be from $e^+e^- \to \gamma\gamma$ events mixing into the pass ZernikeMVA and pass KLM events, so in the future it may be wise to only look at the extrapolation down to $E^* = 6.5\,\text{GeV}$, and not consider the first energy bin. Method 2 results were also removed from the final result. The remaining five numbers were used to put an estimate. Finally, for a duration of roughly 51 days, 15 hours, 26 minutes, and 22 seconds in experiment 12, there are 590 ± 112 cosmic events expected to be remaining for a candidate photon with $4.9\,\text{GeV} < E^* \leq 5.5\,\text{GeV}$ after applying all of the necessary cuts to remove cosmic events.

Chapter 4

Conclusions

4.1 Dark photon search at Belle II

The dark photon is a dark sector mediator which could be produced at e^+e^- colliders. Due to its high luminosity and low trigger threshold, the Belle II experiment can look at sensitivity regions for dark photons that have never been explored before. The signature for this dark photon is $e^+e^- \to \gamma A'$, where only a single recoil photon is left behind in an event. The search is restricted to the dark photon mass of up to $m_{A'} = 10.58\,\mathrm{GeV/c^2}$, which comes from the center of mass energy of the SuperKEKB collider.

The analysis is currently conducted separately for three different regions depending on the dark photon mass, and the analysis described here was for one of the regions with a light dark photon with high single photon energy of $4.9\,\mathrm{GeV} < E^* \leq 5.5\,\mathrm{GeV}$. The dominant background for this signature is $e^+e^- \to \gamma\gamma$, where one of the photons is missed by the detector. In order to study the likelihood of missing photons through both the sub-detectors ECL and KLM, an efficiency study was conducted for different leakage energies using the background control sample. The first step was identifying regions which had more leakage due to the material gaps of the ECL and KLM. After seeing that the leakage distribution depends on the position of probe particles, a comparison was performed between data and MC. There were two main findings from this study; the KLM efficiency for data is less than MC (0.80 ± 0.08 of MC events found in data), and there was a significantly larger number of high leakage probe photons observed in data than in MC (3.1 ± 0.3 times more entries in data than in MC for $0.1\,\mathrm{GeV} < E < 0.55\,\mathrm{GeV}$ of probe photon). The former problem is currently being updated for experiment 12, where the efficiency differences will be found per theta ID, and in the future when estimating the total number of background events from MC, this number will be scaled accordingly for data. The latter problem prompted different studies. Studies with Bhabha events displayed that the problem was specific to photons, which suggests that the crystals in the ECL have larger crystal gaps than in simulation. This was confirmed by looking at the local phi variable between data and MC. Manually moving the crys-

tals in GEANT4 showed that the number of high leakage probe photons do increase with larger gaps. However, rather than keeping the shifted geometry, due to restrictions of GEANT4, finding the scale factor between data and MC for high leakage probes per theta ID was attempted. The studies is still ongoing for experiment 12 data and MC.

Along with the efficiency studies, analysis was also performed using signal events. The optimal cuts between signal and background were found using the Punzi figure of merit. The finalised cuts optimised for MC13b experiment 10 however did not eliminate many events for MC13b experiment 12, where there was more beam background contamination. This study is ongoing for MC14a run independent events, which is currently showing agreement with the distribution of experiment 10.

In addition to the MC comparisons, data was also studied, however both experiment 10 and 12 showed contamination from cosmic and pin diode events. Cuts were made through optimisation, which was not enough to completely eradicate these events. By using different cuts and methods, the expected cosmic and pin diode events were found. After all cosmic and pin diode cuts are applied, for a duration of roughly 51 days, 15 hours, 26 minutes, and 22 seconds, 590 ± 112 cosmic events are expected to be remaining in data when the candidate photon has energy $4.9\,\text{GeV} \leq E^* < 5.5\,\text{GeV}$. The data and MC comparison will be performed on experiment 12 after the cosmic and pin diode events are eliminated from data in the future.

The analysis presented here marks the foundational investigation necessary to understand background events for the dark photon search. This is the first step before proceeding to an analysis to search and discover or set upper limits on the dark photon production at Belle II, which will be the next step of this analysis.

Bibliography

[1] R. D. Peccei and Helen R. Quinn. CP Conservation in the Presence of Instantons. *Phys. Rev. Lett.*, 38:1440–1443, 1977.

[2] Wikipedia contributors. Standard Model, 2021. [Online; accessed 24-August-2021].

[3] Heinz Andernach and Fritz Zwicky. English and Spanish Translation of Zwicky's (1933) The Redshift of Extragalactic Nebulae, 2017.

[4] Rubin, Vera C. and Ford, W. Kent, Jr. Rotation of the Andromeda Nebula from a Spectroscopic Survey of Emission Regions. , 159:379, February 1970.

[5] M. S. Roberts and A. H. Rots. Comparison of Rotation Curves of Different Galaxy Types. , 26:483–485, August 1973.

[6] N. Aghanim, Y. Akrami, M. Ashdown, J. Aumont, C. Baccigalupi, M. Ballardini, A. J. Banday, R. B. Barreiro, N. Bartolo, and et al. Planck 2018 results. *Astronomy Astrophysics*, 641:A6, Sep 2020.

[7] Fiorenza Donato. Indirect searches for dark matter. *Physics of the Dark Universe*, 4:41–43, 2014. DARK TAUP2013.

[8] Carlos Pérez de los Heros. Status of direct and indirect dark matter searches, 2020.

[9] Christopher Karwin, Simona Murgia, Tim M.P. Tait, Troy A. Porter, and Philip Tanedo. Dark matter interpretation of the Fermi -LAT observation toward the Galactic Center. *Physical Review D*, 95(10), May 2017.

[10] O. Adriani, G. C. Barbarino, G. A. Bazilevskaya, R. Bellotti, M. Boezio, E. A. Bogomolov, L. Bonechi, M. Bongi, V. Bonvicini, S. Bottai, and et al. An anomalous positron abundance in cosmic rays with energies 1.5–100gev. *Nature*, 458(7238):607–609, Apr 2009.

[11] M. Aguilar, G. Alberti, Behcet Alpat, Antonio Alvino, Giovanni Ambrosi, Karen Andeen, H. Anderhub, Luisa Arruda, Philipp Azzarello, A Bachlechner, Fernando Barao, B. Baret, Aurelien Barrau, L. Barrin, Alessandro Bartoloni, L. Basara, A. Basili, L. Batalha, J. Bates, and C. Zurbach. First result from the alpha magnetic spectrometer on the international space station: Precision measurement of the positron fraction in primary cosmic rays of 0.5-350 gev. *Phys. Rev. Lett.*, 110:141102, 04 2013.

[12] R. Khatiwada et al. Axion Dark Matter eXperiment: Detailed Design and Operations. 9 2020.

[13] Bob Holdom. Two u(1)'s and charge shifts. *Physics Letters B*, 166(2):196–198, 1986.

[14] Alessandra Filippi and M. De Napoli. Searching in the dark: the hunt for the dark photon. *Reviews in Physics*, 5:100042, 2020.

[15] Matt Graham, Christopher Hearty, and Mike Williams. Searches for dark photons at accelerators. *Annual Review of Nuclear and Particle Science*, 71(1):null, 2021.

[16] Kazunori Akai, Kazuro Furukawa, and Haruyo Koiso. SuperKEKB collider. *Nuclear Instruments and Methods in Physics Research Section A: Accelerators, Spectrometers, Detectors and Associated Equipment*, 907, 08 2018.

[17] DESY. Belle II. `https://www.belle2.org/`.

[18] P.M. Lewis, I. Jaegle, H. Nakayama, A. Aloisio, F. Ameli, M. Barrett, A. Beaulieu, L. Bosisio, P. Branchini, T.E. Browder, and et al. First measurements of beam backgrounds at SuperKEKB. *Nuclear Instruments and Methods in Physics Research Section A: Accelerators, Spectrometers, Detectors and Associated Equipment*, 914:69–144, Jan 2019.

[19] Antonio Paladino. Beam Background at SuperKEKB During Phase 2 Operation. In *62nd ICFA Advanced Beam Dynamics Workshop on High Luminosity Circular e^+e^- Colliders*, 4 2019.

[20] Thomas Browder. Super KEKB and Belle II. `https://www.belle2.org/project/super_kekb_and_belle_ii`.

[21] Laura Zani and Professor Francesco Forti. *Search for an invisible Z' in $\mu^+\mu^-$ plus missing energy events at Belle II.* PhD thesis, Pisa, University of Pisa, Physics Department E. Fermi, Pisa, 2020. Presented on 24 01 2020.

[22] I. Adachi, T. E. Browder, P. Križan, S. Tanaka, and Y. Ushiroda. Detectors for extreme luminosity: Belle II. *Nucl. Instrum. Meth. A*, 907:46–59, 2018.

[23] W. Altmannshofer et al. The Belle II Physics Book. *PTEP*, 2019(12):123C01, 2019. [Erratum: PTEP 2020, 029201 (2020)].

[24] B. Spruck and for BelleII PXD DEPFET collaboration. Belle II Pixel Detector Commissioning and Operational Experience. Feb 2020. The 28th International Workshop on Vertex Detectors PoS(Vertex2019)015 https://pos.sissa.it/373/015/pdf.

[25] T. Abe et al. Belle II Technical Design Report. 11 2010.

[26] Tomohisa Uchida, Masahiro Ikeno, Yoshihito Iwasaki, Masatoshi Saito, Shoichi Shimazaki, Manobu Tanaka, Nanae Taniguchi, and Shoji Uno. Readout electronics for the central drift chamber of the Belle II detector. In *2011 IEEE Nuclear Science Symposium and Medical Imaging Conference*, 2011.

[27] Giacomo De Pietro, Paolo Branchini, and Enrico Graziani. *Search for an invisibly decaying Z' dark boson at Belle II in $e^+e^- \to \mu^+\mu^-(e^\pm\mu^\mp)$ + missing energy final states.* PhD thesis, Rome, Università degli Studi.

[28] M. Akatsu et al. Time of propagation Cherenkov counter for particle identification. *Nucl. Instrum. Meth. A*, 440:124–135, 2000.

[29] Umberto Tamponi. The TOP counter of Belle II: status and first results. 11 2018.

[30] M. Staric. Pattern recognition for the time-of-propagation counter. *Nucl. Instrum. Meth. A*, 639:252–255, 2011.

[31] S. Sandilya. Particle Identification with the TOP and ARICH detectors at Belle II. 2017.

[32] Saint-Gobain. CsI(Tl) Thallium activated Cesium Iodide. `https://www.crystals.saint-gobain.com/products/csitl-cesium-iodide-thallium`.

[33] B. Shwartz. Electromagnetic calorimeter of the Belle II detector. *J. Phys. Conf. Ser.*, 928(1):012021, 2017.

[34] I. Adachi, T. E. Browder, P. Križan, S. Tanaka, and Y. Ushiroda. Detectors for extreme luminosity: Belle II. *Nucl. Instrum. Meth. A*, 907:46–59, 2018.

[35] Michael De Nuccio. The Belle II Electromagnetic Calorimeter. `https://indico.belle2.org/event/99/sessions/52/attachments/1009/1557/2019_June_SK_TFMDN_4.pdf`.

[36] Y. Makida, H. Yamaoka, Y. Doi, J. Haba, F. Takasaki, and A. Yamamoto. Development of a superconducting solenoid magnet system for the B factory detector (BELLE). *Adv. Cryog. Eng.*, 43:221–228, 1998.

[37] Yoshihito Iwasaki, ByungGu Cheon, Eunil Won, Xin Gao, Luca Macchiarulo, Kurtis Nishimura, and Gary Varner. Level 1 trigger system for the Belle II experiment. *IEEE Trans. Nucl. Sci.*, 58:1807–1815, 2011.

[38] Steffen Baehr, S. Skambraks, S. Neuhaus, C. Kiesling, and J. Becker. A neural network on FPGAs for the z-vertex track trigger in Belle II. *JINST*, 12(03):C03065, 2017.

[39] S. Lee, R. Itoh, N. Katayama, and S. Mineo. Development of high level trigger software for Belle II at SuperKEKB. *J. Phys. Conf. Ser.*, 331:022015, 2011.

[40] J. P. Lees et al. Search for Invisible Decays of a Dark Photon Produced in e^+e^- Collisions at BaBar. *Phys. Rev. Lett.*, 119(13):131804, 2017.

[41] D. Banerjee, V.E. Burtsev, A.G. Chumakov, D. Cooke, P. Crivelli, E. Depero, A.V. Dermenev, S.V. Donskov, R.R. Dusaev, T. Enik, and et al. Dark Matter Search in Missing Energy Events with NA64. *Physical Review Letters*, 123(12), Sep 2019.

[42] Sam Cunliffe, Torben Ferber, Christopher Hearty, and Miho Wakai. Search for single photon events: plots for approval for ICHEP2020, BELLE2-NOTE-PH-2020-050. Jun 2020.

[43] C.M. Carloni Calame, G. Montagna, O. Nicrosini, and F. Piccinini. The BABAYAGA event generator. *Nuclear Physics B - Proceedings Supplements*, 131:48–55, 2004. SIGHADO3.

[44] D. Y. Kim et al. The simulation library of the Belle II software system. *J. Phys. Conf. Ser.*, 898(4):042043, 2017.

[45] Johan Alwall, Michel Herquet, Fabio Maltoni, Olivier Mattelaer, and Tim Stelzer. MadGraph 5: going beyond. *Journal of High Energy Physics*, 2011(6), Jun 2011.

[46] T. Kuhr, C. Pulvermacher, M. Ritter, T. Hauth, and N. Braun. The Belle II Core Software. *Computing and Software for Big Science*, 3(1), Nov 2018.

[47] Francesco Tenchini. MC13 low multiplicity samples at Y(4S) for single-photon analysis. `https://agira.desy.de/browse/BIIDP-2195`.

[48] Marco Melesi. Processing 2019a-b-c. `https://confluence.desy.de/display/BI/Processing+2019a-b-c#Processing2019a-b-c-FilelocationatKEKCC`.

[49] Jake Bennet. Processing 2019a-b. `https://confluence.desy.de/display/BI/Processing+2019a-b#Processing2019a-b-Processing10details`.

[50] Jake Bennet. Processing 2019c. `https://confluence.desy.de/display/BI/Processing+2019c`.

[51] Stefano Lacaprara. Processing 2020a-b. `https://confluence.desy.de/display/BI/Processing+2020a-b`.

[52] Christopher Hearty. Alignment of the Belle II calorimeter using muon pairs, BELLE2-NOTE-TE-2020-031. Dec 2020.

[53] Giovanni Punzi. Sensitivity of searches for new signals and its optimization. *eConf*, C030908:MODT002, 2003.

[54] Alon Hershenhorn, Torben Ferber, and Christopher Hearty. ECL shower shape variables based on Zernike moments, BELLE2-NOTE-TE-2017-001. Jan 2017.

[55] The SciPy community. scipy.stats.kstest. `https://docs.scipy.org/doc/scipy/reference/generated/scipy.stats.kstest.html`.

Appendix A

Analysis on cosmic events

A.1 ZernikeMVA and KLM cuts for data

The table was used to predict the number of cosmic events that will pass both the ZernikeMVA cut and the best KLM layer cut for data. The number that was being predicted is the empty entry for PassZ PassK with $4.9\,\text{GeV} \leq E^* < 5.5\,\text{GeV}$ for the candidate photon. Each entry represents the number of events that passed the corresponding cuts using Bucket 9-15 Exp12 data.

Energy Distribution	**PassZ FailK**	**PassK FailZ**	**PassZ PassK**	**FailZ FailK**
$4.9\,\text{GeV} \leq E^* < 5.5\,\text{GeV}$	17622 ± 133	25543 ± 160		206909 ± 455
$5.5\,\text{GeV} \leq E^* < 6.5\,\text{GeV}$	13251 ± 115	30277 ± 174	1291 ± 36	242229 ± 492
$6.5\,\text{GeV} \leq E^* < 7.5\,\text{GeV}$	8891 ± 94	20660 ± 144	521 ± 23	163355 ± 404
$7.5\,\text{GeV} \leq E^* < 8.5\,\text{GeV}$	6558 ± 81	15175 ± 123	343 ± 19	115955 ± 341
$8.5\,\text{GeV} \leq E^* < 9.5\,\text{GeV}$	4773 ± 69	11510 ± 107	291 ± 17	86066 ± 293
$9.5\,\text{GeV} \leq E^* < 10.5\,\text{GeV}$	3802 ± 62	8780 ± 94	217 ± 15	65522 ± 256
$10.5\,\text{GeV} \leq E^* < 11.5\,\text{GeV}$	2954 ± 54	7059 ± 84	162 ± 13	51731 ± 22
$11.5\,\text{GeV} \leq E^* < 12.5\,\text{GeV}$	2285 ± 48	5872 ± 77	153 ± 12	41561 ± 204
$12.5\,\text{GeV} \leq E^* < 13.5\,\text{GeV}$	1777 ± 42	4788 ± 69	128 ± 11	34209 ± 185
$13.5\,\text{GeV} \leq E^* < 14.5\,\text{GeV}$	1468 ± 38	4090 ± 64	94 ± 10	28381 ± 168
$14.5\,\text{GeV} \leq E^* < 15.5\,\text{GeV}$	1146 ± 34	3432 ± 59	78 ± 9	23463 ± 153
$15.5\,\text{GeV} \leq E^* < 16.5\,\text{GeV}$	921 ± 30	3603 ± 60	76 ± 9	26067 ± 161
$16.5\,\text{GeV} \leq E^* < 17.5\,\text{GeV}$	789 ± 28	4240 ± 65	37 ± 6	18627 ± 169
$17.5\,\text{GeV} \leq E^* < 18.5\,\text{GeV}$	504 ± 22	3262 ± 57	35 ± 6	21349 ± 146
$18.5\,\text{GeV} \leq E^* < 19.5\,\text{GeV}$	389 ± 20	2995 ± 55	38 ± 6	17837 ± 134
$19.5\,\text{GeV} \leq E^* < 20.5\,\text{GeV}$	278 ± 17	2681 ± 52	18 ± 4	15316 ± 124
$20.5\,\text{GeV} \leq E^* < 21.5\,\text{GeV}$	164 ± 13	2392 ± 49	14 ± 4	12544 ± 122
$21.5\,\text{GeV} \leq E^* < 22.5\,\text{GeV}$	156 ± 12	2390 ± 44	20 ± 4	11636 ± 108
$22.5\,\text{GeV} \leq E^* < 23.5\,\text{GeV}$	102 ± 10	1936 ± 44	17 ± 4	8788 ± 94
$23.5\,\text{GeV} \leq E^* < 24.5\,\text{GeV}$	35 ± 6	761 ± 28	4 ± 2	3260 ± 57

Table A.1: Table for the number of events which pass and fail the ZernikeMVA and KLM cut for Buckets 9-15 Exp 12 data.

A.2 ZernikeMVA and KLM cuts for cosmic events

The table shows the number of cosmic events that passed the corresponding cuts using experiment 16 and 18 cosmic events. This table was used to predict the number of cosmic events that will pass both the ZernikeMVA cut and the best KLM layer cut for data.

Energy Distribution	**PassZ FailK**	**PassK FailZ**	**PassZ PassK**	**FailZ FailK**
$4.9\,\text{GeV} \leq E^* < 5.5\,\text{GeV}$	595 ± 24	1207 ± 35	32 ± 6	14150 ± 119
$5.5\,\text{GeV} \leq E^* < 6.5\,\text{GeV}$	716 ± 27	1428 ± 38	34 ± 6	17048 ± 131
$6.5\,\text{GeV} \leq E^* < 7.5\,\text{GeV}$	495 ± 22	1009 ± 32	36 ± 6	11265 ± 106
$7.5\,\text{GeV} \leq E^* < 8.5\,\text{GeV}$	341 ± 18	793 ± 28	22 ± 5	8108 ± 90
$8.5\,\text{GeV} \leq E^* < 9.5\,\text{GeV}$	251 ± 16	600 ± 24	18 ± 4	5920 ± 77
$9.5\,\text{GeV} \leq E^* < 10.5\,\text{GeV}$	199 ± 14	466 ± 22	12 ± 3	4607 ± 68
$10.5\,\text{GeV} \leq E^* < 11.5\,\text{GeV}$	164 ± 13	331 ± 18	6 ± 2	3699 ± 61
$11.5\,\text{GeV} \leq E^* < 12.5\,\text{GeV}$	104 ± 10	326 ± 18	8 ± 3	3024 ± 55
$12.5\,\text{GeV} \leq E^* < 13.5\,\text{GeV}$	103 ± 10	248 ± 16	4 ± 2	2292 ± 48
$13.5\,\text{GeV} \leq E^* < 14.5\,\text{GeV}$	72 ± 8	198 ± 14	3 ± 2	2015 ± 45
$14.5\,\text{GeV} \leq E^* < 15.5\,\text{GeV}$	67 ± 8	185 ± 14	2 ± 1	1690 ± 41
$15.5\,\text{GeV} \leq E^* < 16.5\,\text{GeV}$	53 ± 7	187 ± 14	5 ± 2	1876 ± 43
$16.5\,\text{GeV} \leq E^* < 17.5\,\text{GeV}$	34 ± 6	233 ± 15	2 ± 1	2159 ± 46
$17.5\,\text{GeV} \leq E^* < 18.5\,\text{GeV}$	30 ± 5	195 ± 14	0 ± 0	1509 ± 39
$18.5\,\text{GeV} \leq E^* < 19.5\,\text{GeV}$	19 ± 4	179 ± 13	0 ± 0	1270 ± 36
$19.5\,\text{GeV} \leq E^* < 20.5\,\text{GeV}$	12 ± 3	155 ± 12	2 ± 1	1076 ± 33
$20.5\,\text{GeV} \leq E^* < 21.5\,\text{GeV}$	4 ± 2	133 ± 12	1 ± 1	932 ± 31
$21.5\,\text{GeV} \leq E^* < 22.5\,\text{GeV}$	8 ± 3	136 ± 12	0 ± 0	891 ± 30
$22.5\,\text{GeV} \leq E^* < 23.5\,\text{GeV}$	7 ± 3	117 ± 11	1 ± 1	659 ± 26
$23.5\,\text{GeV} \leq E^* < 24.5\,\text{GeV}$	5 ± 2	46 ± 7	0 ± 0	264 ± 16

Table A.2: Table for the number of events which pass and fail the ZernikeMVA and KLM cut for cosmics events in Exp16 and Exp18.